UNIVERSITY OF OKLAHOMA

GRADUATE COLLEGE

RF MODELING AND ELECTROMAGNETIC ANALYSIS OF IMPLANTABLE DEVICES IN MAGNETIC RESONANCE IMAGING

A DISSERTATION

SUBMITTED TO THE GRADUATE FACULTY

in partial fulfillment of the requirements for the

Degree of

DOCTOR OF PHILOSOPHY

By

SATTAR ATASH BAHAR
Norman, Oklahoma
2017

RF MODELING AND ELECTROMAGNETIC ANALYSIS OF
IMPLANTABLE DEVICES IN MAGNETIC RESONANCE IMAGING

A DISSERTATION APPROVED FOR THE
SCHOOL OF ELECTRICAL AND COMPUTER ENGINEERING

BY

Dr. Hjalti H. Sigmarsson, Chair

Dr. Jorge Salazar-Cerreño

Dr. Rockee Zhang

Dr. Caleb Fulton

Dr. Royce W. Floyd

This dissertation is dedicated to my family.

Acknowledgments

The completion of this work would not have been possible without the help and encouragement of many people. First, I would like to thank my advisor Hjalti Sigmarsson for all his guidance and support. I would also like to thank Professors Jorge Salazar-Cerreño, Rockee Zhang, Caleb Fulton and Royce W. Floyd for serving on my advisory committee.

I also sincerely thank David Thompson, Director of Emerging Technology at LivaNova, for his support, discussions and guidance throughout my research. I am particularly grateful to him for the opportunity he provided me to conduct independent research.

Special thanks go to Sasidhar Vajha and James Pierpont for their support, discussions, and help during the course of this work. I would also like to acknowledge my colleagues, members of Neuromodulation group at LivaNova: Kenny Henderson, Rajesh Ramesh, Ashwini Reddy, and Olutosin Fawole.

For assistance with the fabrication of the prototypes I would like to thank Michael Gaines and Daniel Hernandez. I also wish to thanks Dr. John Murphy, Vice president of R&D at LivaNova for his support of this work.

I am grateful to the financial support for my research by LivaNova.

Table of Contents

List of Tables

List of Figures

Abstract

Magnetic Resonance Imaging (MRI) has become a generally accepted medical procedure and it is estimated that all the U.S. population will have at least one MRI scan in their lifetime. Unlike common radiography and computed tomography, MRI has many advantages including its nonionizing nature and the capability to distinguish soft tissues. However, the substantial benefits of MRI are often not available to patients with implanted medical devices, such as a pacemaker, an implantable cardiovascular device, a deep brain stimulator, or a neurostimulator.

MRIs utilize three powerful fields in the process of producing images, static field, gradient field and Radio Frequency (RF) field that coexist during the scanning. The interaction between the implantable device and the RF electromagnetic field is the main hazard during MRI scanning for most active implantable medical devices. The conductive parts, mainly, the lead wire, act like antennas that pick up the available incident energy. This may result in excessive heating with the capacity for tissue damage [1], [2]. Moreover, the RF power delivered to the Implantable Pulse Generator (IPG) is another concern as it can damage the internal circuitry [3], [4].

In this research, a comprehensive model of the implant in the presence of MRI RF waves is presented. This circuit model represents the induced current and is used to design a lead that minimizes the coupled power to the IPG. This

model significantly simplifies designing a new lead by removing Electromagnetic (EM) simulation of implantable devices inside the human body. Also, a circuit model is introduced that extracts the transfer function from the measured parameters of the lead. A miniaturized RF power measurement setup that conforms to the IPG case is designed and used to measure the coupled RF power to the IPG without using external components. This method of measurement, improves the accuracy of the measurement and can be used to measure RF coupled power to the antenna. For communication to the implant using Bluetooth technology, an antenna is designed and the effectiveness of the new measurement setup for the coupled MRI RF waves to the antenna port is demonstrated.

Chapter 1

Introduction

1.1 Overview

Magnetic Resonance Imaging (MRI) has become one of the most important non-invasive clinical diagnostic tools to produce high-resolution image of human tissue [5], [6]. While MRI is considered a very safe method that has no long term effects, there are in fact some limitation regarding its usage in a group of patients. Those with a conductive or a magnetic implantable medical device, which is the subject of interest, belongs to this category. The number of patients with medical implantable devices like, cardiac pace maker and neurostimulation systems like deep brain stimulator and Vagus nerve stimulator is growing rapidly every year [7], [8].

Static field, gradient field and Radio Frequency (RF) field are generated in any MRI device during the process of producing images. and they are coexist at the same time. Depending on the strength of the magnetic field, which could be 1.5 T or 3 T, the RF frequency is 64 MHz or 128 MHz, respectively, which is equal to the Larmor frequency at the aforementioned strength of magnetic field. The interaction between the implantable device and RF electromagnetic field is the main hazard during the MRI scanning for most active implantable

medical devices. The lead wire with the IPG case, acts like an antenna that picks up the RF energy. This may result in excessive heating with the capacity for tissue damage especially at the wire's tip, where the RF energy will concentrated. Moreover, the RF voltage delivered to the IPG is another concern that can damage the internal circuitry. This is a complicated challenge that depends on multiple parameters including the surrounding tissue, MRI scanner frequency and MRI RF power, position of the implantable device, lead path, lead design, and lead length [9], [10].

A complete model that predicts the RF behavior is a fundamental key for understanding the interaction between the implantable device and the MRI RF signal. This model could be a circuit model or a simplified Electromagnetic (EM) model that predicts the transmission and radiation performance.

Figure 1.1 shows an AspireSR, the first and only Vagus nerve therapy that provides responsive stimulation to heart rate increase inside the human body. The IPG case, which also called can is installed under the skin over the chest and the lead connects the pulse generator to the nerve. The lead needs to be long enough to connect the IPG to the nerve in different human body types. The path and the depth of the lead could vary, which will change the RF heating. Moreover, there could be a loop in the path as well that changes the interaction with MRI RF. To find the maximum potential heating, a comprehensive study of the likely paths is needed. The lead has two electrodes that deliver the voltage to the nerve and an anchor that holds the lead in place.

1.1.1 Implantable device in MRI

The interaction between the MRI RF field and the conductive implantable device inside the human body transfers energy as heat to the surrounding tissue

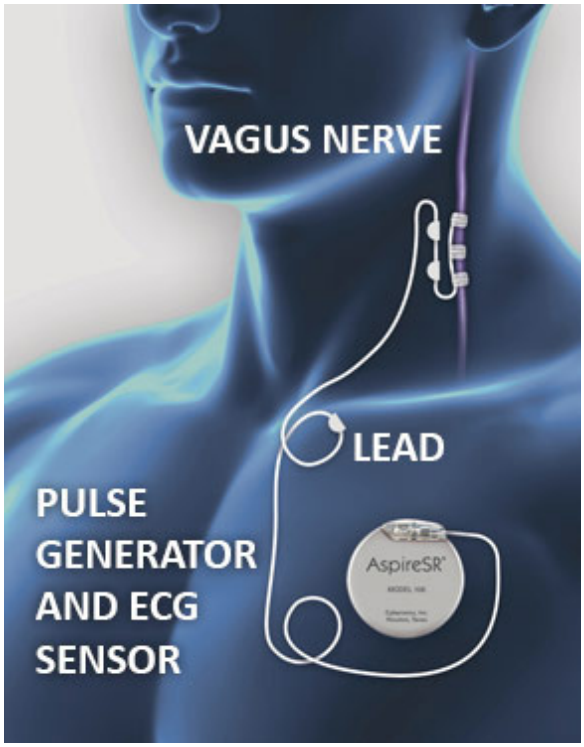

Figure 1.1: Vagus nerve stimulator inside a human body that shows the three main parts: pulse generator, lead and electrodes (from [8]).

and delivers RF voltage to the IPG. The amount of heating mainly depends on the lead's parameters. Although, we study the lead at high frequencies, the main task of the lead is to deliver the low frequency signals from the pulse generator to the nerve. The majority of the frequency content of the signal for therapy is below 200 Hz.

In addition to the RF characteristics, there are multiple criteria that need to be considered while designing the lead. Depending on the model and the purpose of the IPG, the device should be able to work inside the human body for approximately 5 years, or more, with the same battery and without any additional surgery. Therefore, the dissipated power in the lead at low frequencies is a crucial factor and an important parameter on the longevity of the device. The lower the dissipated power is, the longer the device will work due to the

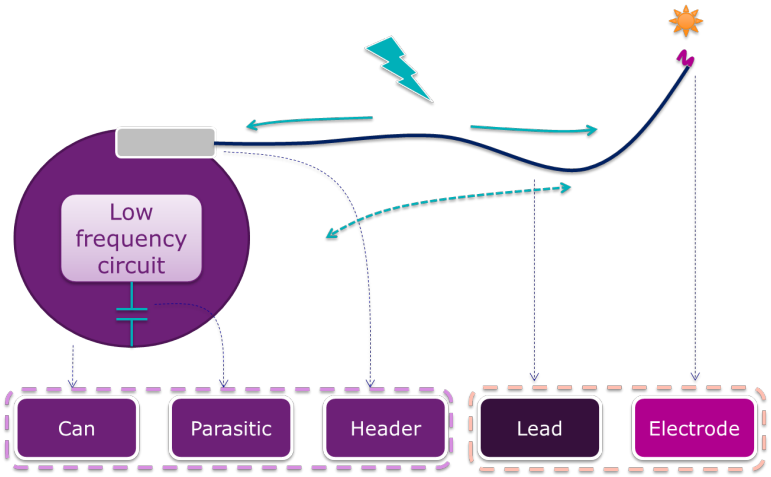

Figure 1.2: Structure of an implantable device that contains the parts affected by the RF interaction.

lower battery drain. Moreover, the lead needs to be mechanically durable to the stresses for the years of operation. The lead connects the IPG, which is placed in the sub-clavicle region of the chest, to the vagues nerve. The conductors inside the lead must sustain the stress and pressure from the neck and chest movements. Moreover, all the used materials need to be bio-compatible. These are the main restrictions in designing a lead.

An implantable device that contains the parts affected by the RF interaction is shown in Figure 1.2. The low frequency circuit inside the IPG produces the signal for the therapy. The output of this circuit is connected to the lead using a technothane header and filtered feed-through. The lead delivers the signal to the nerve using the electrodes. The feed-through capacitor inside the header, shunts the high frequency signal to the IPG case and prevents damaging the internal circuit from induced currents on the lead due to external fields.

The maximum temperature rise occurs where the scattered electric field is maximum. Usually, the tip of an open ended electrode is where the maximum

coupled power is dissipated. However, all parts of the implantable device need to be modeled for a comprehensive understanding of the interaction due to the RF field. Each component of the implant that interacts with the electric field may change the electrical length and therefore the Self Resonant Frequency (SRF). This variation results in an alteration of the magnitude of the induced current.

1.2 Background of MRI safe implantable devices

There are multiple factors related to MRI RF heating. The exterior parameters are the bore diameter, bore length, field strength, type of the sequence, position, and geometry of the implanted device inside human body, as well as the position and posture of the body inside the scanner [1]. Calculating or measuring of magnitude and phase of the electrical field in the medium is the first step in this study. It is possible to find the electric field components using simulation software or using a probe in an MRI. A specific hazard for excessive tissue heating during MRI arises if the conductive implants align with the electric field in the body. No significant implant heating occurs in positions with low overall electric field strength or if the implant is positioned orthogonal to the local electric field. Distribution of the amplitude of electric fields inside the human body-like phantom in an MRI scanner is shown in Figure 1.3.

In addition to the exterior parameters, the wire shape, length, and material that is used in the designing the lead has a significant impact on the RF heating [2]–[4]. A wire length study and the impact of the heating of a nitinol guidewire was investigated in [11]. The SRF of conductors is a mechanisms by which heating can be extracted. However, it is difficult to predict because it strongly depends on the surrounding tissue of the lead or guid-wire. For

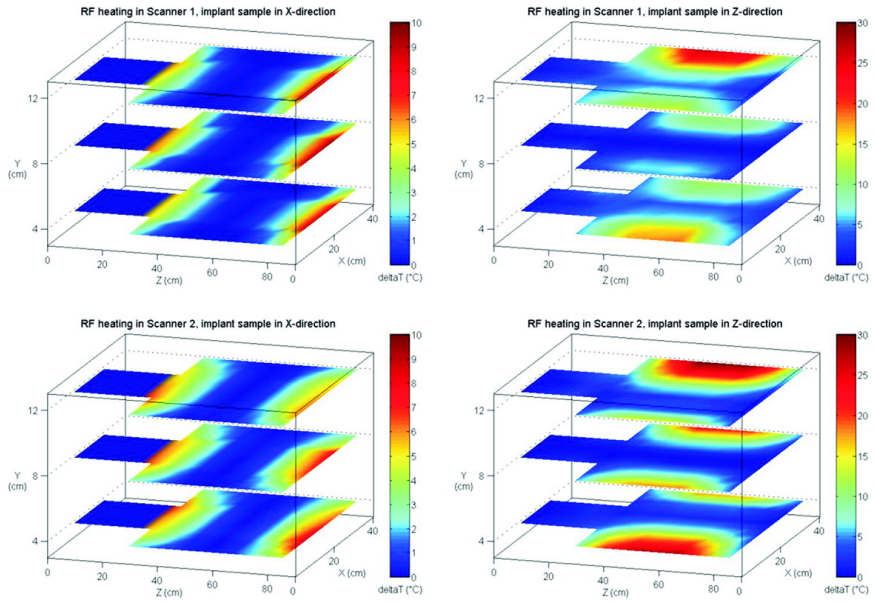

Figure 1.3: Spatial distribution of induced electric fields within the human-body-like phantom liquid in an MRI scanner (from [1]).

example, the heating that may be produced on a resonating guide-wire is not an intrinsic item of the wire, but depends on a large and rather poorly defined set of environmental factors. The permittivity of the lead's surrounding tissue may vary from 4 to 86 inside the human body. Therefore, the amplitude and phase of the incident electrical field will change as well. Moreover, the resonant frequency of the structure is also a function of the tissue. The problem becomes more challenging when the lead crosses multiple tissues with different parameters.

The center conductor of the guide-wire acts like an antenna and is excited by the radiated electric field. At same time, it acts like the core of a transverse electromagnetic (TEM) waveguide. The wave reflects at the ends and in some specific situations, the superimposed TEM waves form a standing wave and the electrical field near the guide-wire causes the displacement current in the layer directly surrounding the wire. The resonating length equals:

$$L \approx n * \frac{\lambda_{TEM}}{2}, n = 1, 2, 3, ... \tag{1.1}$$

and as mentioned, depends on multiple parameters.

The magnitude of the heating is proportional to the amount of dissipated energy, which corresponds to the Specific Absorption Rate (SAR) from the induced current. This value is extracted using the Electromagnetic (EM) simulator and a safety index (°C/(W/kg)) is introduced, which is the temperature measurement normalized to SAR of the pulse sequence. This method is applicable to both insulated and non-insulated wires that are completely inserted in the human body, such as wire leads for pacemakers, neurostimulators, and spinal fusion stimulators [12]. Figure 1.4 shows the theoretically predicted safety index for different variations of bare wire diameter, insulation thickness, relative permittivity of the insulation, and electrical conductivity of the tissue. SAR depends on the coil geometry and the properties of the tissue and can be calculated using the following equation:

$$SAR = \frac{\sigma E^2}{2\rho_t} \tag{1.2}$$

where E is the amplitude of electric field, σ is the electrical conductivity and ρ_t is the mass density of the tissue.

Another method to investigate temperature rising on the implantable devices is based on the impedance of the EM wave. An impedance match between the radiated RF signal and the lead common mode can cause heating at the near tip. Adding a filtering circuit that forms a high impedance structure, reduces the common mode current and limits the amount of heating. However, in this case, the SRF of the lead can be excited which maximizes the induced

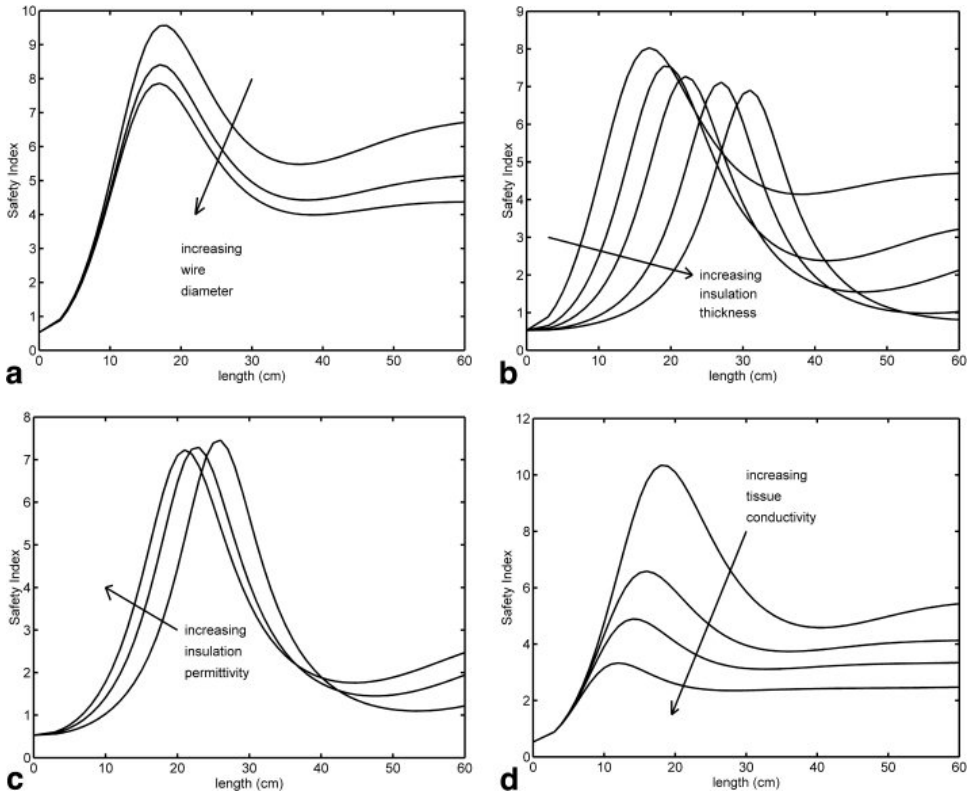

Figure 1.4: Theoretically predicted safety index (from [12]).

current. Dividing the long conductor into multiple short sections, increases the SRF and suppresses the common mode effects [7]. Figure 1.5 shows the measured SRF in a standard line and a line with a filter. The minimum resonant frequency increased from 41.4 MHz to 103 MHz and the weakly coupled method of measuring the SRF, eliminates the importance of the amplitude of S_{11}. It is known from antenna theory that by adding a capacitor along the length of an antenna, that the first resonant frequency can be increased. However, this method is not applicable when the lead needs to deliver the low frequency signal from IPG to the targeted nerve.

Calculation of the heating along the lead has been investigated using different methods [3], [6], [9], [10], [13]–[18].

Temperature increase on the lead is a function of both the transfer function

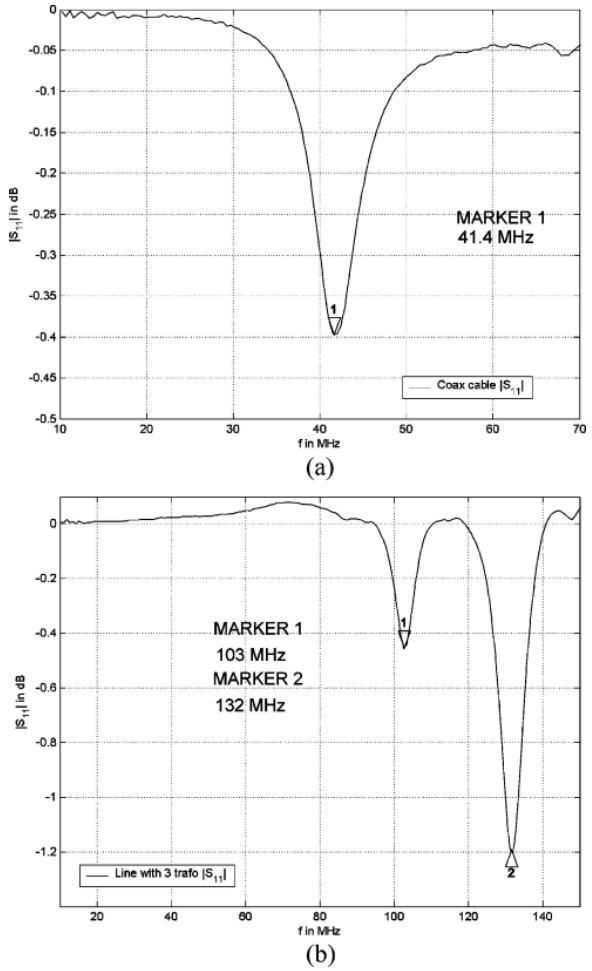

Figure 1.5: Self-resonant frequency shift in. S_{11} for a) standard line and b) with the transformer line, both fully immersed in water (from [7]).

and the incident electric field along the lead [14]. Figure 1.6 shows the concept of the lead's transfer function. The tangential electric field E_{tan} is coupled along the length (L) of the lead. τ is the distance from the electrode and P is the position vector of the evaluation point. The scattered field related to the incident field by the transfer function $S(\tau, P)$

$$E_s(P) = \int_0^L S(\tau, P)\, E_{tan}(\tau)\, d\tau. \tag{1.3}$$

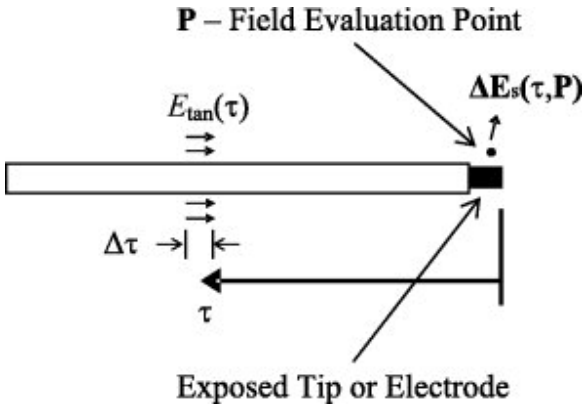

Figure 1.6: Transfer function method and scattered electric field near the electrode. With knowledge of the transfer function, the local SAR can be calculated (from [14]).

The scattered electric field is independent from the E_{tan} and with knowledge of the transfer function, the local SAR can be calculated and therefore the temperature rise at a point P near the electrode.

EM simulation can be used to extract the transfer function. In the presence of the MRI RF field that induces current along the lead, a scattered electric field from this current at the test point P is calculated. The radial component of the scattered electric field is equivalent to E_{tan} [12]. The transfer function of the lead depends on the surrounding environment and frequency [19], [20]. Due to the complexity of the lead, usually a simple wire is used to extract the transfer function. Figure 1.7 shows the measured and calculated temperature increase over time. This method is used to validate the transfer function method.

For communication to implantable devices, antennas have been designed for different purposes and at multiple frequencies [21]–[27]. One of the main frequencies that these antennas are designed at is 400 MHz for telemetry, communication and power transfer applications. Moreover, implantable antennas for communication at 2.4 GHz ISM band have been designed [28], [29].

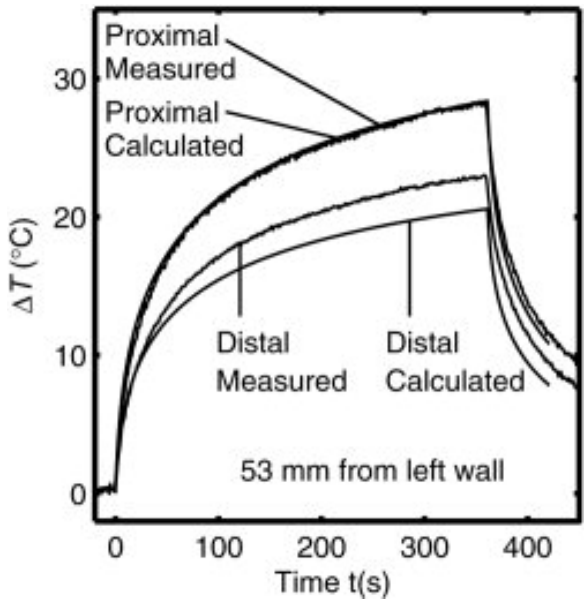

Figure 1.7: Measured and calculated temperature increase vs. time for validation of the transfer function method (from [14]).

However, antenna radiation performance at MRI RF frequencies has not been considered and the coupled RF energy during the MRI scanning has not been measured.

1.3 MRI conditional safe implantable devices

To reduce the risk of hazardous heating from RF excitation, multiple methods has been investigated. RF chokes that filter the MRI RF signal with a length of quarter wave length were used to reduce the currents induced on the cable shield [30]. This method is used to reduce the heating due to the SRF of Intravascular Catheters.

An MRI conditional safe brain stimulator lead based on resistive tapered strip-line technology is introduced in [31]. This design breaks up the induced RF current along the lead as well as dissipating power. Consequently, the

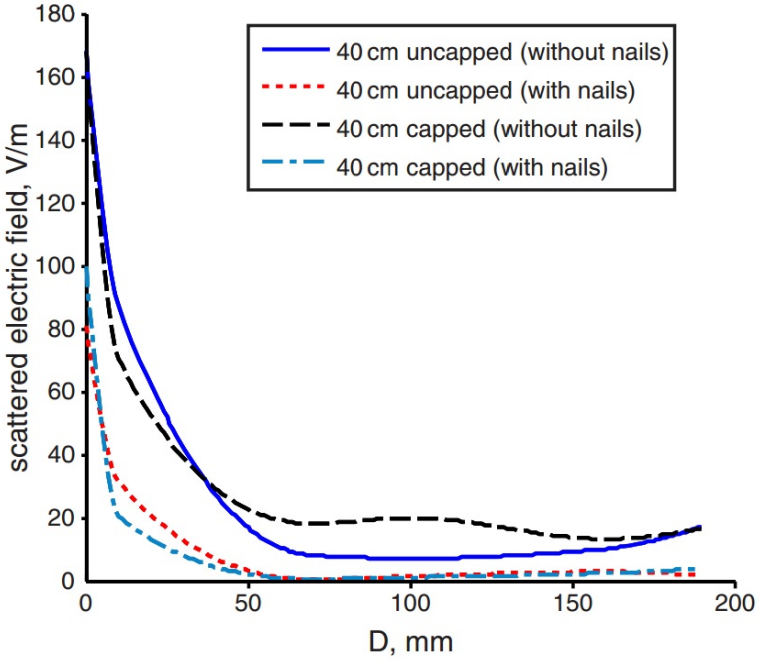

Figure 1.8: Electric field reduction at the tip by implementing nails along the lead (from [32]).

temperature increase at the electrode is limited.

During the MRI scanning, strong electric field can exist at the lead tip. Due to the low conductivity of the surrounding tissue, the stored energy in the scattered electric field is transfered to heat. A medical lead implant with nails to reduce the scattered field near the lead tip is introduced in [32]. The electric field strength reduction using the nails is shown in Figure 1.8. The distance of the RF excitation from the tip is shown on the horizontal axis as D. The graph presents the scattered electric field for both capped and uncapped situations while the length of the lead is constant.

Bio-compatible Nickel-Titanium alloy T-shaped pins has been placed along the lead to reduce the RF heating. The distance between the pin's head and the existing lead forms parallel capacitors that can be controlled using the dimensions of the pin. Usually a coil is placed near the lead tip which forms

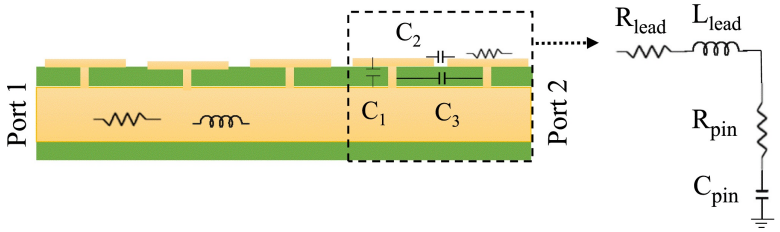

Figure 1.9: T-shaped bio-compatible lead and circuit model (from [9]).

a low-pass frequency response filter with the pins [9]. The structure and the equivalent circuit are shown in Figure 1.9. Due to the complexity of the lead, a wire is used in this simulation. The wire diameter is 1.6 mm and the insulator diameter is 2.5 mm.

A modified transmission line model has been introduced in [16], [33] that models the induced current along the lead during MRI. Series voltage sources are placed between transmission line unit cells to model distributed excitation of an external field. Moreover, IPG case and electrode are modeled with a voltage source and an impedance. In this method, traditional ways of determining transmission line parameters are neither valid nor simple to derive for complex lead geometries.

A deep brain stimulator that has helical coils along the lead with non-uniform diameters was presented in [5]. The transmission line properties of the lead vary by changing the helical coil diameter. Therefore, the lead's characteristic impedance at the MRI frequency can be increased. Controlling these parameters results in reduced amplitude of the induced currents.

1.4 Research objective

The work presented here addresses modeling of implantable devices in the presence of MRI RF waves. For extracting the transfer function of the lead, a

new method to measure transmission line parameters of the lead in saline is presented. Using this model, the impedance, resistivity, and electrical length of the lead are extracted. Moreover, a circuit model to extract the transfer function based on the transmission line is introduced.

To prevent implant malfunction during MRI, coupled energy to the IPG needs to be measured and its value should be less than the maximum power handling of the modules inside the IPG. A new method is designed and implemented based on a miniaturized measurement setup to measure coupled MRI RF power to the IPG. All analog and digital circuitry is placed in the implant. This method provides an accurate tool for malfunction tests performed on all of the IPG ports.

For communication to the implant, an antenna is designed and fabricated based on the position of the IPG inside the human body. Sensitivity of the implant antenna to the variation of the human body is provided using EM simulations. The MRI RF coupled energy is measured using the new method that is introduced in this work.

Finally, a circuit model of the implant inside human body during MRI scanning is introduced. The conventional transmission line model is expanded to model the induced current and the external radiated RF field in MRI. Using this model, the current and voltage along multiple leads are provided. This method removes the time consuming EM simulations during the development of new leads. Moreover, a parsed transmission line unit cell is introduced which provides two degrees of freedoms in lead design.

Overall, this research provides a new methodology and concepts for modeling implantable devices. These methods enable systematic design of the next generation of implantable devices and can be used to solve significant health

risks for patients undergoing MRI scanning. The new state-of-the-art methods for modeling implantable devices and the expansion of the fundamental concepts of transmission line theory, for addressing challenges associated with current and future MRI technologies, are the main contributions of this work.

Chapter 2

Measurement methods of coupled MRI RF signal to implantable devices

During MRI scanning, high power signals couples to the lead. The signal that delivered to the IPG can cause malfunction in the device. The purpose of this portion of the project is to demonstrate different methods of measuring the coupled voltage on the lead. In this chapter two methods are introduced to measure the amount of power or voltage that couples to the lead and therefore to the IPG. This value then will be injected into the device for the malfunction test.

2.1 Implantable devices inside the MRI

To measure the coupled signal into an implantable devices, based on the state-of-the-art method, a voltage sensor is used [34] where the lead is connected to the IPG. The measurement setup is placed outside the IPG and the measured data is transfered to outside of the shielded room. However, there are multiple drawbacks using this method to measure the coupled voltage. The measurement setup is exposed to the MRI RF field. The interaction of the RF field and measurement setup could change the coupled signal value that depends on the position of the measurement setup. Moreover, the interaction

of the digital circuit of the measurement setup and the high power RF signal could result in malfunction of the measurement circuit. Finally, the exposing wires of the measurement setup to the RF signal adds more uncertainty to the measurement results.

In this chapter a novel method for measuring the signal coupled an into implantable device during the MRI scanning is introduced. This method can be used for measuring the RF power induced on the lead or the antenna of implantable devices. This approach uses an Internal RF Power Detector (IRPD) that covers all the MRI RF frequencies. All the data is recorded in the internal memory inside the implantable device during the measurement and then extracted after the MRI scanning.

2.2 Methodology

A block diagram of the proposed measurement setup is shown in Figure 2.1. All the measurement setup components are placed inside the implantable device to minimize the interaction between the MRI RF fields and the IRPD. The measurement setup is designed and fabricated on a Printed Circuit Board (PCB) that is the same size as the original IPG PCB. The two halves of the IPG case are sealed and covered using copper tape. Recorded data is extracted after the test by taking the IRPD out of the IPG. The measurement setup has main four sections including, an attenuator network, an RF power detector, a micro-controller and memory as described below.

The received signal level inside the IPG depends on multiple parameters that include the input impedance of the IPG load that can be transceiver module or Application-Specific Integrated Circuit (ASIC) and the impedance of the coupled source to the IPG, that can be the lead or the antenna. The attenuator

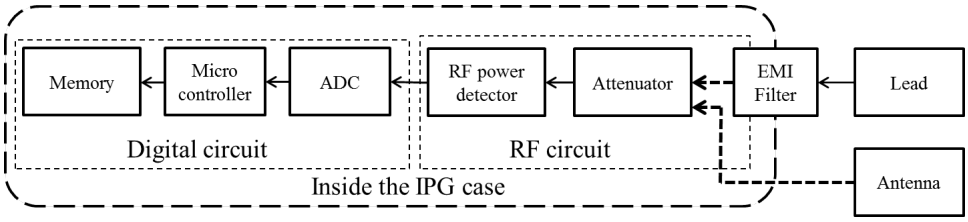

Figure 2.1: Block diagram of the proposed IRPD. Coupled RF signal to the implantable device from the lead or antenna is delivered to the RF power detector. The microcontroller records the output DC of the RF detector using the internal ADC.

network is placed before the IRPD to reduce the received power level to fit within the operating range of the RF detector.

The coupled RF power is measured using an available RMS power detector, ADL5906 from Analog Devices. The frequency range of operation is 10 MHz to 10 GHz and the dynamic range is more than 60 dB. The input impedance is 50 Ohm. The time response is optimized to detect the maximum power level for a sinc pulse shape. The output of the detector is a DC voltage proportional to the RF power. Moreover, temperature compensation is enabled to minimize the effects of potential variation on the board temperature during the MRI scanning.

The analog output DC value of the RF power detector is digitized using a 10 bit ADC. The ADC is an internal feature of the selected microcontroller from Atmel. The ATmega324P is a low-power CMOS 8-bit microcontroller that has 8 channel 10 bit ADC and 1 KB internal memory or EEPROM. Sampled data is recorded in the memory and extracted after the experiment.

2.2.1 Algorithm

The IRPD is designed and fabricated on a board that is the same size as the implanted device circuit board. The IRPD is placed inside the case and

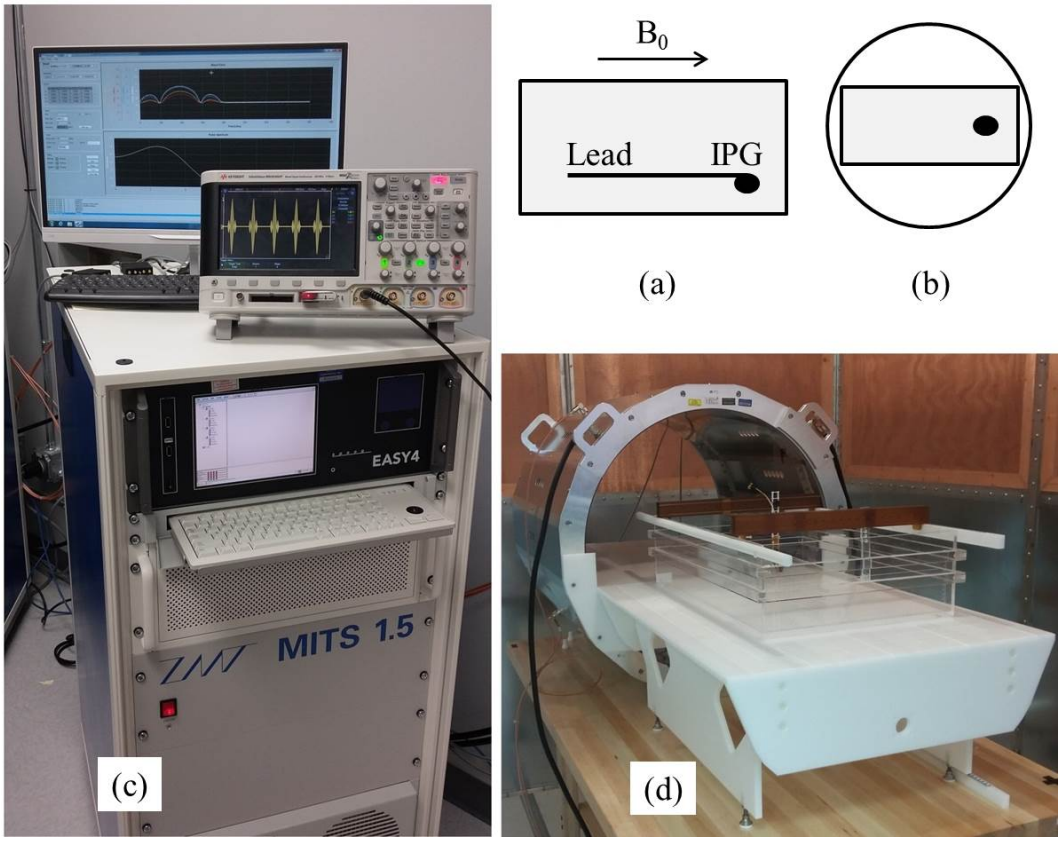

Figure 2.2: MRI RF birdcage setup and placement of the IPG and lead. (a) Top view of the birdcage that shows the lead where the distance from edge is 4 cm. (b) Side of the birdcage where the IPG is placed at the center. (c) The console of MRI RF coil. (d) Medical test implant system 1.5 T

powered using an internal battery. The current consumption of the RF power detector is 68 mA. There is a one hour delay before the power detector is turned on. This is the time needed after the board is powered up and placed inside the case. At this time the microcontroller is in sleep mode and the RF detector is off. In the sleep mode, the total current consumption at this period is less than 2 mA. The microcontroller starts sampling the signal at the ADC pin. Before writing the maximum value in the EEPROM, the value is compared with the stored value and if it is higher then it will be replaced. This processes continues until the board is powered off. In this method, the

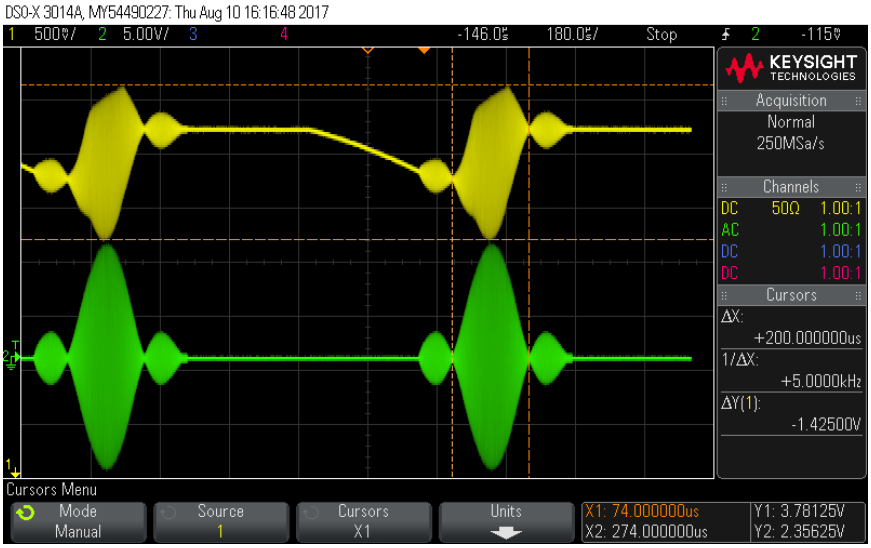

Figure 2.3: Pulse width measurement and output of the RF detector

Table 2.1: IRPD characterization

Injected signal		Measured signal			
Freq (MHz)		64		128	
PW(dBm)	Volt(mV)	Osc.	ADC	Osc.	ADC
-55	0.398	0.57	0.69	0.59	0.7
-50	0.707	0.74	0.76	0.81	0.82
-40	2.236	1.26	1.22	1.33	1.29
-30	7.071	1.82	1.77	1.9	1.85
-20	22.36	2.39	2.32	2.48	2.4

memory behaves like a maximum hold and it will be rewritten if the next value is higher than the stored value.

To erase the EEPROM between the measurements and sending the recorded data to the serial port, two switches are implemented on the board. After the MRI test, the IPG case is opened and recorded data is transfered through the serial port.

2.3 Characterization of ADC

The RF power detector response with the internal ADC is calibrated using a bench desk setup. A SMC100A from Rohde & Schwarz and an Agilent E4418B are used as the RF signal generator and the power meter, respectively. Two signals at different power levels for both 64 MHz and 128 MHz are injected into the RF power detector. A KEYSIGHT 33500B waveform generator is used as an external source to modulate the RF signal. The DC output of the RF detector is measured using the oscilloscope and the internal ADC. The result of the measurement is shown in Table 2.1. The internal reference voltage of the microcontroller is 2.56 mV which limits the detectable voltage. The 10 bit ADC provides the accuracy of 2.5 mV/bit which corresponds to the 0.045 dB/bit. The minimum detectable signal without noise is -55 dBm. Without any external network, the RF power detector and ADC provide 40 dB of dynamic range, however, the maximum detectable power can be increased by using an external attenuator.

Based on the RF power detector datasheet, the RMS averaging capacitor (CRMS) provides the averaging function for the internal RMS computation. Using the minimum value for CRMS allows the quickest response time to a pulsed waveform but leaves significant output noise on the output voltage signal. However, a large filter capacitor reduces output noise but at the expense of response time. The recommended value for the CRMS is 0.1 μF which ensures good RMS accuracy for this signal type. All the other necessary components for the RF power detector are based on the Figure 51 in [35].

The time domain response of the IRPD is characterized using the MRI RF birdcage signal. The placement of IPG inside the saline is shown in Figure 2.2 (a) and Figure 2.2 (b). The MRI RF birdcage and its controller are

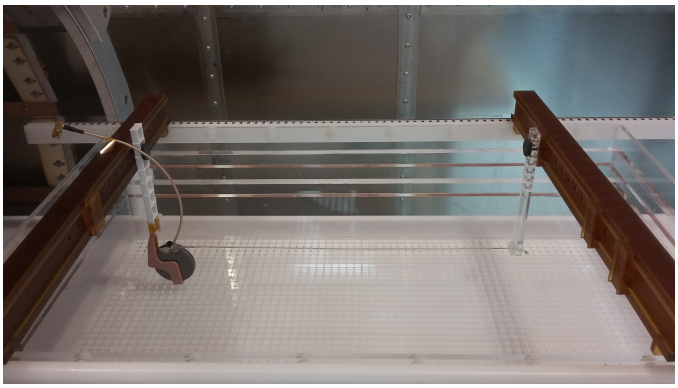

Figure 2.4: Coaxial cable setup for measuring the coupled signal. A half wave coaxial cable connected to the high impedance port of a oscilloscope.

shown in Figure 2.2 (c) and Figure 2.2 (d), respectively. The antenna is placed inside the RF birdcage and the received signal is transmitted outside of the shielding room using a coaxial cable and injected into the RF power detector. Both the RF signal and the corresponding DC output value of the RF power detector are shown in Figure 2.3. The test signal is a sinc function, 90 deg circular polarized with a Pulse Repetition Rate (PRR) of 1 KHz and a duty cycle of 40%.

2.4 Microcontroller program

The ADC, memory and micro-controller are implemented in the same chip. When the battery is connected to the IRPD, it takes about half an hour to place it inside the IPG case and prepare it for the MRI measurement. The initial step in the program sets the microcontroller in idle mode and turns the RF power detector off. This step is using the minimum power consumption, which is less than 2 mA and saves the battery for the measurement. The microcontroller starts sampling the DC output of the RF power detector. This process continues in a loop and when it reaches the end of the EEPROM, it

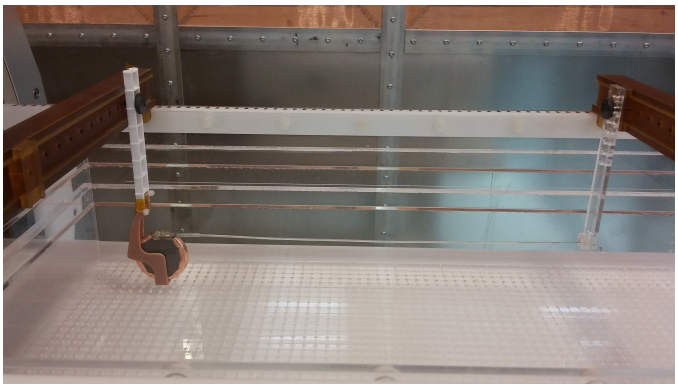

Figure 2.5: RF measurement setup using the internal power detector. In this setup no external component is added for the measurement.

returns to the start of the memory.

Two switches are placed at the board for sending the data to the serial port and to reset the EEPROM data. After each measurement EEPROM is erased to have value of zero in the memory.

2.5 Measurement of coupled MRI RF signal

The coupled RF power into the implantable device is measured in the medical test implant system and MRI RF birdcage as shown in the Figure 2.2. All tests are conducted in both available 64 MHz and 128 MHz birdcages, which have the maximum output RF power of 46 dBm and 60.2 dBm, respectively.

2.5.1 Lead measurement

A pulse generator prototype lead based on the work in[36] with the implantable device as shown in Figure 2.4 is used for this measurement. The input impedance of the prototype lead is measured at the IPG connection point and it is 72.46 ohm and 51.37 ohm at 64 MHz and 128 MHz, receptively. The measurement is in air at a fixed position while the RF power level is changed.

The recorded data in the EEPROM is shown in the Figure 2.7 and Figure 2.8 for 64 MHz and 128 MHz, respectively. This data shows the values recorded in the internal memory at different times for different power levels.The extracted maximum voltage data versus radiated power levels are shown in the Table 2.2 and Table 2.3 for 128 MHz and 64 MHz, respectively.

Using the internal voltage reference of the microcontroller, for the ADC, increases the accuracy of the measurement. However, this method limits the maximum voltage readable from the RF power detector. An attenuator network is implemented to attenuate the received signal and increase the maximum detectable power. The equivalent circuit model of the EMI filter is shown in Figure 2.6. The EMI filter, C_1 in this prototype is 3,700 pF.

2.5.2 Generalized scattering parameter

The EMI filter is placed between lead and internal circuit as shown in Figure 2.6 (a). Due to the impedance differences at both sides of the filter, the insertion loss needs to be calculated using the generalized scattering matrix. The equivalent circuit model is shown in Figure 2.6 (b). Lead and the internal circuitry of IPG are the two ports of this model. Impedance of each port are denoted by Z_p.

$$a = \frac{1}{2}k\left(V + Z_p I\right) \tag{2.1}$$

$$b = \frac{1}{2}k\left(V - Z_p^* I\right) \tag{2.2}$$

where, wave number k is

$$k = \left(\sqrt{|Re\left\{Z_p\right\}|}\right)^{-1} \tag{2.3}$$

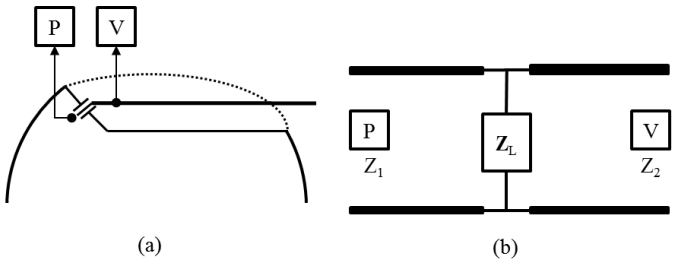

Figure 2.6: IPG circuit and EMI filter. (a) IPG schematic where the voltage (V) and power (P) are measured. (b) Equivalent circuit model.

and a and b are the complex amplitude of incident and exiting wave from the port, respectively. The voltage and the current at each transmission line termination can be written as:

$$V_i = V_i^+ + V_i^- \tag{2.4}$$

$$I_i = Y_0 \left(I_i^+ - I_i^- \right) \tag{2.5}$$

Then the scattering parameters can be computed directly using the following formula:

$$S_{ij} = \frac{V_i^-}{V_j^+}|_{v_k^+ = 0 \forall k \neq j} \tag{2.6}$$

Consider (2.6) at the junction of the two transmission lines the voltage is continuous and the currents differ:

$$V_1 = V_2 \tag{2.7}$$

$$I_1 + I_2 = Y_L V_2 \tag{2.8}$$

To compute S_{11} after the terminating port 2 the $V_2^+ = 0$. The above equation

can be rewritten as:

$$Y_1\left(V_1^+ - V_1^-\right) + Y_2\left(-V_2^-\right) = Y_L V_2^- \tag{2.9}$$

$$Y_1\left(V_1^+ - V_1^-\right) = \left(Y_2 + Y_L\right) V_2^- \tag{2.10}$$

$$V_2^- = \frac{Y_1\left(V_1^+ - V_1^-\right)}{\left(Y_2^- + Y_L\right)} \tag{2.11}$$

using the $V_1^+ + V_1^- = V_2^-$:

$$V_1^- = V_2^- - V_1^+ \tag{2.12}$$

$$V_1^- = \frac{Y_1\left(V_1^+ - V_1^-\right)}{\left(Y_2^- + Y_L\right)} + V_1^+ \tag{2.13}$$

after simplification:

$$V_1^-\left(Y_1 + \left(Y_L + Y_2\right)\right) = V_1^+\left(Y_1 - \left(Y_L + Y_2\right)\right) \tag{2.14}$$

and the return loss:

$$S_{11} = \frac{V_1^-}{V_1^+} = \frac{Y_1 - \left(Y_L + Y_2\right)}{Y_1 + \left(Y_L + Y_2\right)} \tag{2.15}$$

since $V_2^- = V_1^+ + V_1^-$ and $S_{21} = V_2^-/V_1^+$ insertion loss can be written as:

$$S_{21} = 1 + S_{11} = \frac{2Y_1}{Y_1 + \left(Y_L + Y_2\right)} \tag{2.16}$$

2.5.3 EMI filter insertion loss

The measured coupled voltage on the lead is shown in Figure 2.6 (a) and denoted by V and the power is measured inside the IPG and denoted by P. The insertion loss of the EMI filter, based on the measured data, is 53.88 dB

Table 2.2: Measured voltage versus the RF power input in 3 T MRI birdcage

Power in dBm (V)	Pk-Pk Coax (V)	Meas voltage (V)
39.2	1.45	1.47
42.2	2.03	1.51
48.2	4.02	1.67
54.2	8	1.96

Table 2.3: Measured voltage versus the RF power input in 1.5 T birdcage

Power in dBm (V)	Pk-Pk Coax (V)	Meas voltage (V)
37	1.09	1.047
40	1.53	1.064
43	2.25	1.099
46	3.26	1.159

and 50.01 dB for 64 MHz and 128 MHz, respectively.

2.6 Conclusion

In this chapter a novel method to measure the coupled MRI RF signal into the implantable devices using an internal RF power detector circuit is demonstrated and the results are verified using the coaxial cable method. A miniaturized measurement setup can be designed which makes it compatible with most implementable devices. Shielded IRPD and digital circuitry of the measurement setup inside the IPG, eliminates the variation of the RF field. Moreover, having all the parts inside the case, removes the uncertainty of the direct coupling to the measurement setup and potential malfunction of the digital circuit. Moreover, this method is used to measure the RF coupled signal into the antenna of the implant. This setup is capable of measuring the RF energy received at the implant ports from exposure to 1.5 T, 3 T and upcoming MRI technologies. Also, by using multiple RF power detectors, it is possible to measure the coupled signal on all the ports simultaneously.

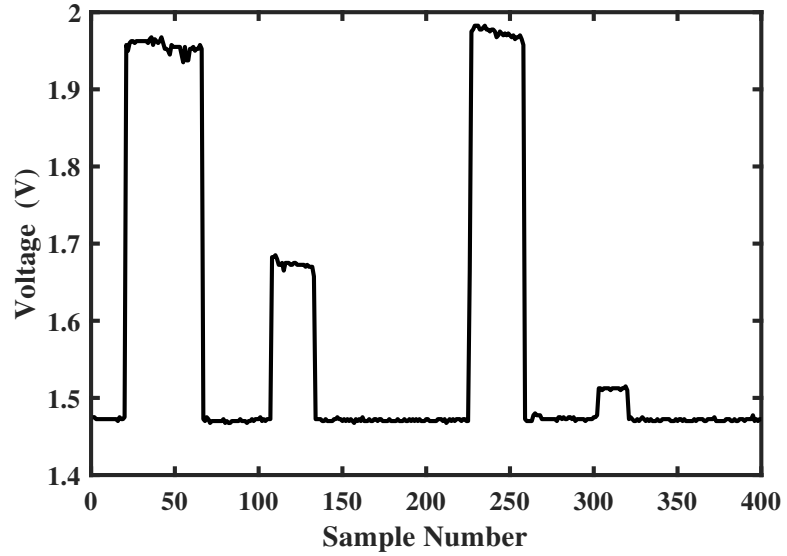

Figure 2.7: Measured data using the RF power detector that recorded in the micro-controller's EEOROM for different RF power level in the 3 T MRI birdcage

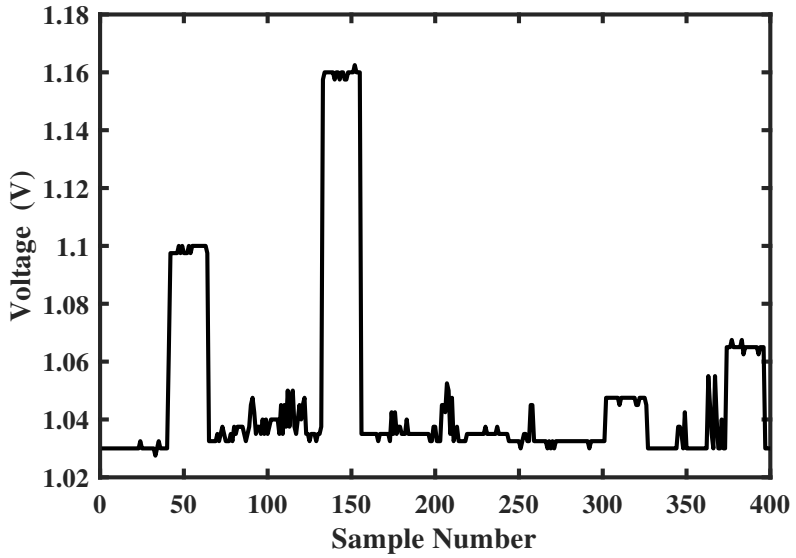

Figure 2.8: Measured data using the RF power detector that recorded in the micro-controller's EEOROM for different RF power level in the 1.5 T MRI birdcage

Chapter 3

Lead transfer function

The purpose of this portion of the research is to demonstrate the transmission line method to calculate the transfer function of the lead. A 10 cm section of the lead is connected to two SMA connectors where mounted on a 10 cm by 10 cm copper plates that serve as the ground planes. The lead is immersed in saline and the two port s-parameters are measured. The equivalent transmission line parameters are extracted. This circuit model can be used to find the transfer function of leads with different lengths and at any frequency.

Moreover, using this method the transfer function can be extracted at any point that is not physically measurable using conventional methods.

3.1 Introduction

To understand the heating in implantable devices during MRI, both experiments and advanced electromagnetic (EM) simulations were performed [37]. It is extremely challenging to solve both human body and lead models in a 3D EM solver due to the sub-millimeter structures of implantable device systems. Moreover, due to the number of required mesh inside the human body, these EM simulations can take days to solve. A transfer function concept was proposed to decouple the micro-scale lead from the macro-level human body

simulation [13], [14]. However, one of the main limitation of this approach is that for finding the transfer function of a lead for different lengths, all of them need to be fabricated and measured. Moreover, this method only provides the capability of measuring transfer functions of leads and not designing one for having a desired transfer function.

3.1.1 Lead heating evaluation using the transfer function method

In this section a common method of evaluating the RF heating on implantable devices based on the transfer function method is described. The steps of this method are described in this section and they are shown in Figure 3.1 [38].

First, an ASTM phantom is simulated with the lead placed in different configurations. The tangential E-field is extracted for each possible configuration of the lead path inside the human body. Second, the temperature rise in the RF birdcage coil is measured for the simulated paths. Third, the current distribution profile on the lead or transfer function is involved and a scaling factor is calculated. The transfer function is validated and used for the heating calculations for different paths and configurations.

3.1.2 Conventional transfer function measurement method

The conventional method for measuring transfer functions is shown in Figure 3.2. In this setup port 1 is the transmitter and port 2 is the receiver. The signal is coupled to the lead using a small gap between the port 1 center conductor and lead conductors as shown in Figure 3.3 and Figure 3.4. To prevent disturbing the current along the lead, weak electromagnetic coupling method is utilized. A current probe is connected to port 2. The current probe

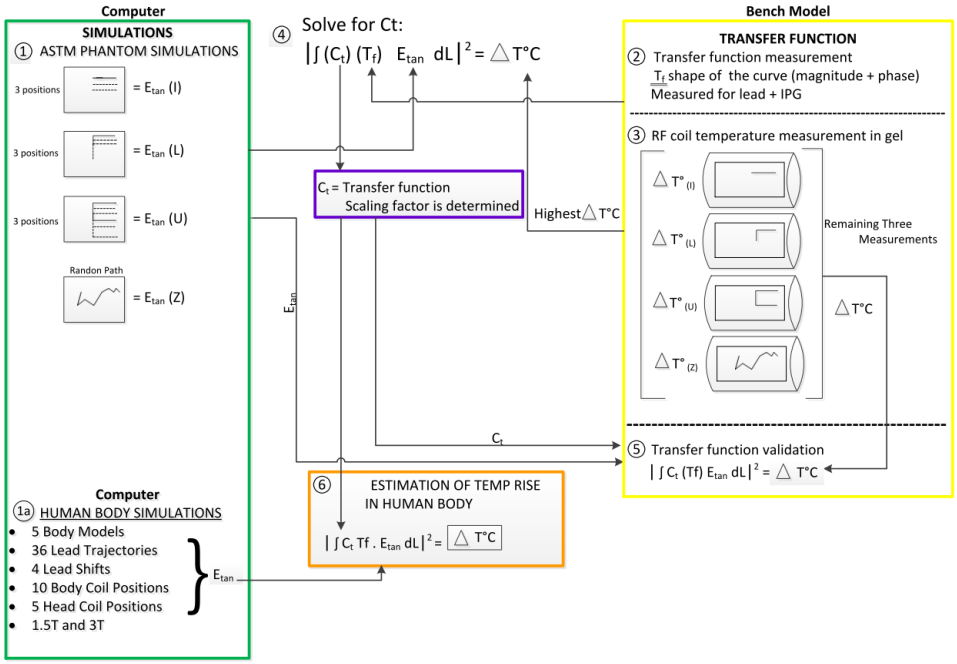

Figure 3.1: Flow chart of RF induced heating assessment using transfer function. (from [39])

is swept from one side of the lead to the other end in 1 cm increments. Simulation results for $-S_{21}$ are shown in Figure 3.5 and Figure 3.6, which are the magnitude and phase of the insertion loss, respectively. Moving the current probe along the lead will impact the impedance and consequently the level of the coupled signal. However, the observed variation in the output reflection coefficient was less than 5%. Therefore, it is negligible and S_{21} does not need to be normalized.

In this chapter, a novel method for deriving and simulating the transfer function of the lead in a circuit simulator is introduced. This method does not require time-consuming EM simulation. Moreover, a transmission line model is developed based on the actual lead that can be used to simulate any lead length.

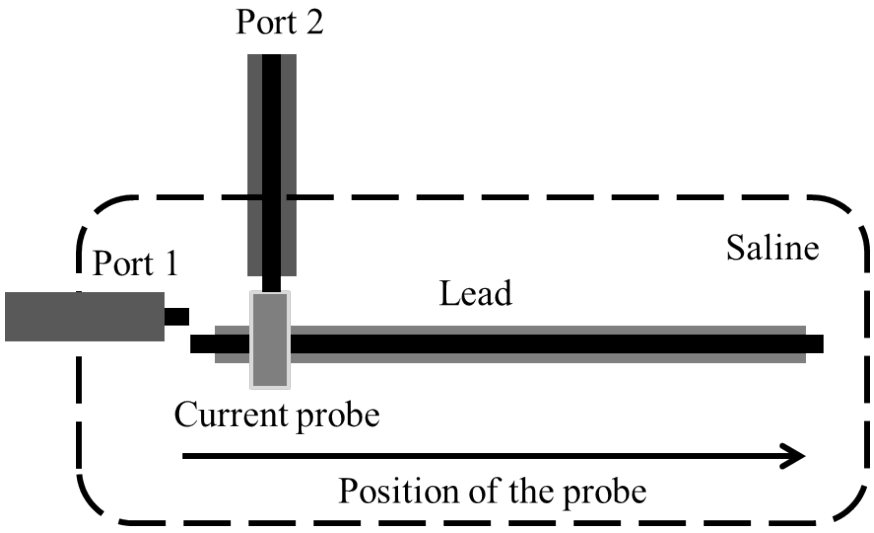

Figure 3.2: Transfer function extraction simulation setup using 3D EM solver. Coupling to port 1 is simulated as a function of the position of port 2.

3.2 Lead transmission line model

To create the lead model, a two-port measurement inside saline with a ground plane is executed as described and showed in Figure 3.7. The SMA inner pin is connected to the 10 cm lead conductor, and the SMA body is placed on a 10 cm by 10 cm copper sheet as the ground plane. The configuration is shown in Figure 3.8. The distance between the lead insulator and the ground plane is sealed using non-conductive glue which guarantees that the saline does not short the lead to the ground plane. The two port s-parameters are measured from 50 MHz to 130 MHz. The model based on this frequency range will be used in both 1.5 T and 3 T MRIs. The saline is at room temperature with a conductivity of 0.47 S/m, which represents the human body. The data is recorded using an Agilent E5062a Vector Network Analyzer (VNA). The two port measurement is calibrated at the end of the cables and before the ground plane. The connection between the VNA cables and setup is sealed to prevent water leakage into the SMA connector.

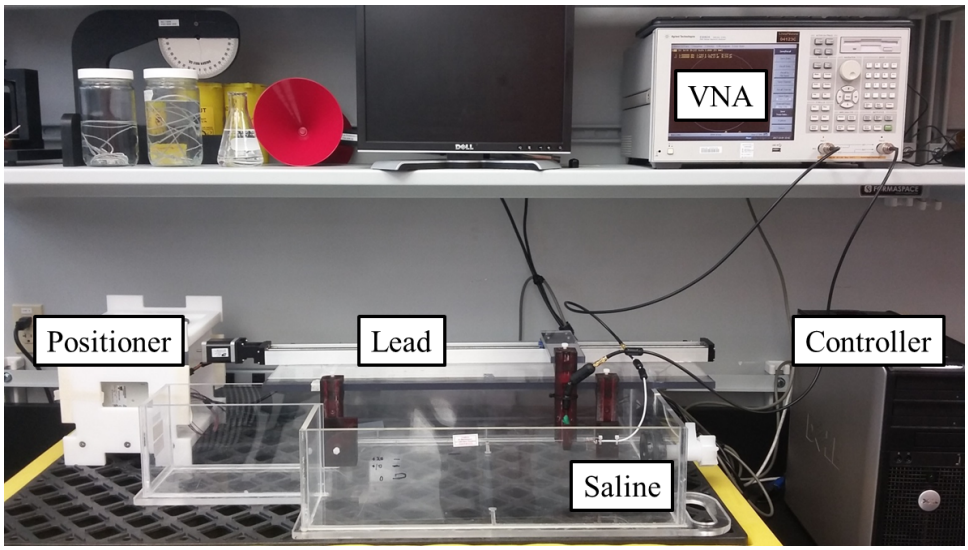

Figure 3.3: Transfer function measurement setup that includes a vector network analyzer for measuring the scattering parameters. A positioner that moves the current probe along the lead and a computer that control the movement and records the data (same method in [38]).

Table 3.1: Transmission line model parameters based on the measurement of the lead inside the saline

R (ohm/m)	L (uH/m)	G(mS/m)	C (pF/m)	Z0
400	1.32	12.6	140	97.1

The measured s-parameters file is imported into the circuit simulator. Ten consecutive TL building blocks are placed between two ports. The frequency range is set from 50 MHz to 130 MHz and the goals is to simulate S_{11}, S_{12}, S_{22} and S_{21} and find the equivalent lumped element parameters of the TL model. Using the available genetic algorithm optimization in the circuit simulator, these parameters are extracted. The simulated and measured results of the TL model are shown in Figure 3.11 and Figure 3.12. The derived transmission line model parameters based on the method presented in this chapter are shown in Table 3.1.

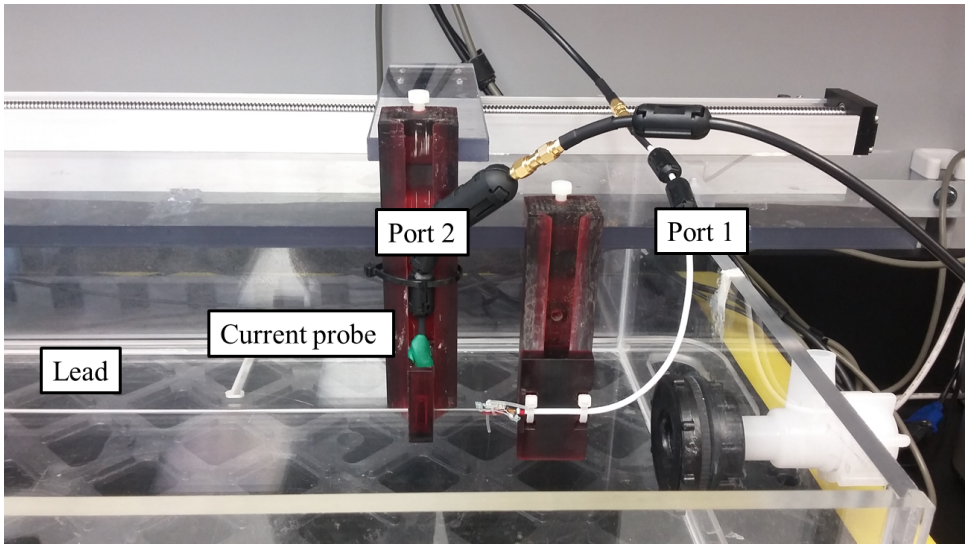

Figure 3.4: Transfer function measurement setup using a network analyzer. Port 1 is weakly coupled to the lead at the end. Port 2 is connected to a current probe. The current probe moves along the lead and S21 is recorded for each point.

3.3 Transfer function

The transfer function can be simulated using the TL model. To find the transfer function with 1 cm resolution, the TL model is divided into multiple sections, as depicted in Figure 3.10. Port 1 is the injecting port of the simulation. The other ports are placed along the lead. To reduce the impact of the ports on the current distribution, the impedance of these ports is set to 20 kΩ. C1 is set to 900 pF, which is proportional to the coupling value in the measurement. The measurement and simulation results of the transfer function at 64 MHz and 128 MHz are shown in Figure 3.13 to Figure 3.16. These graphs show the amplitude and phase of the transfer function that are measured based on the current probe and simulated using the method that is introduced in this chapter.

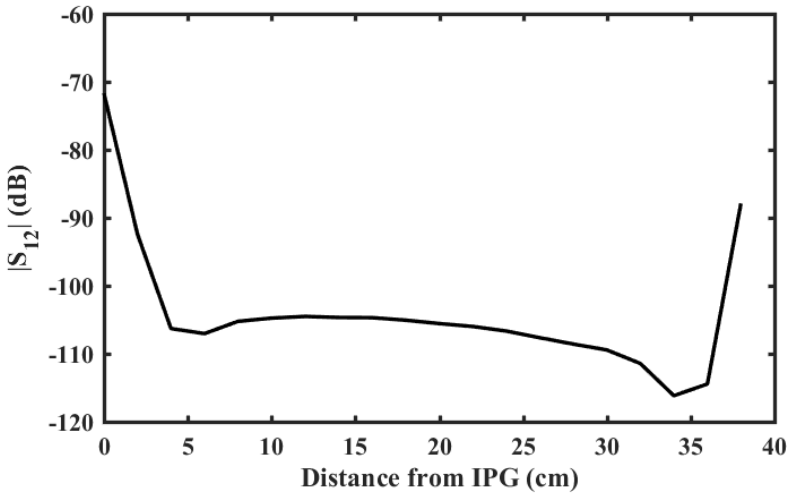

Figure 3.5: Amplitude of transfer function of a straight wire using the EM simulator. The length of the lead is 40 cm where the diameter of the center wire and the outer insulator are 1.6 mm and 2.5 mm, respectively.

3.4 Conclusion

A novel method was developed to find the lead transfer function based on the transmission line model. The primary benefits of this method is that does not require time-consuming EM simulations. The TL model is valid from 50 MHz to 130 MHz and can predict the performance for both 1.5 T and 3 T MRIs. Moreover, along with the developed transfer function, this method provides all the TL parameters that are needed in order to understand the performance of the lead at frequencies which therapy signal is transmitted to the target tissue from the IPG.

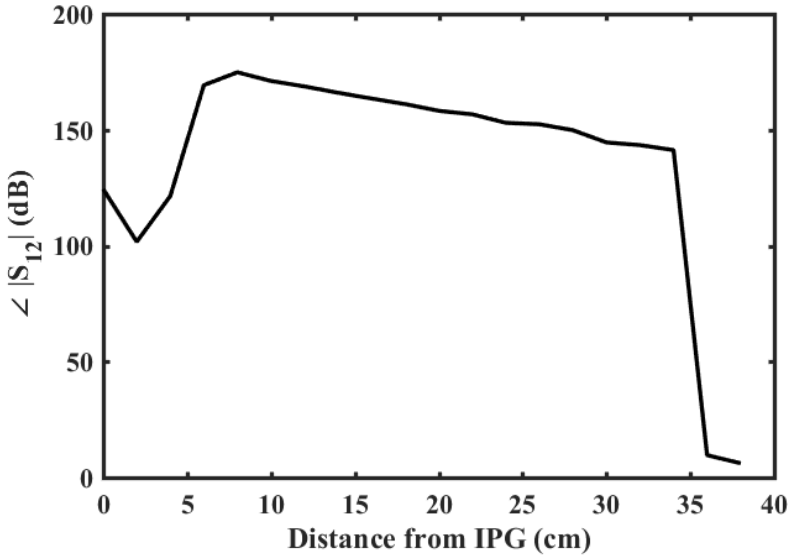

Figure 3.6: Phase of the transfer function of a straight wire using the EM simulator. The length of the lead is 40 cm where the diameter of the center wire and the outer insulator are 1.6 mm and 2.5 mm, respectively.

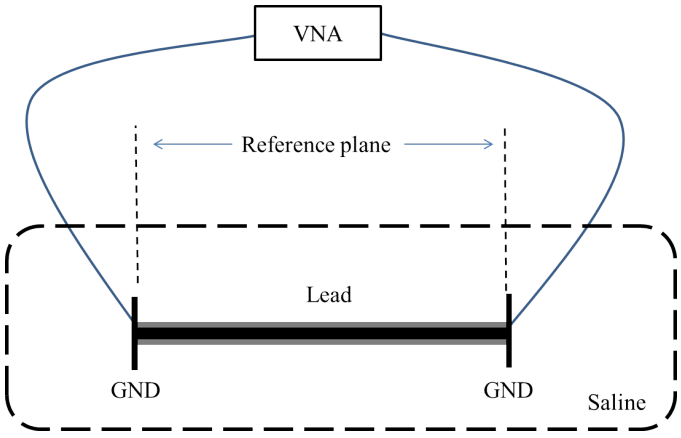

Figure 3.7: Measurement setup of the two port scattering parameters of the lead inside the saline. Two port of the VNA is calibrated at the reference planes.

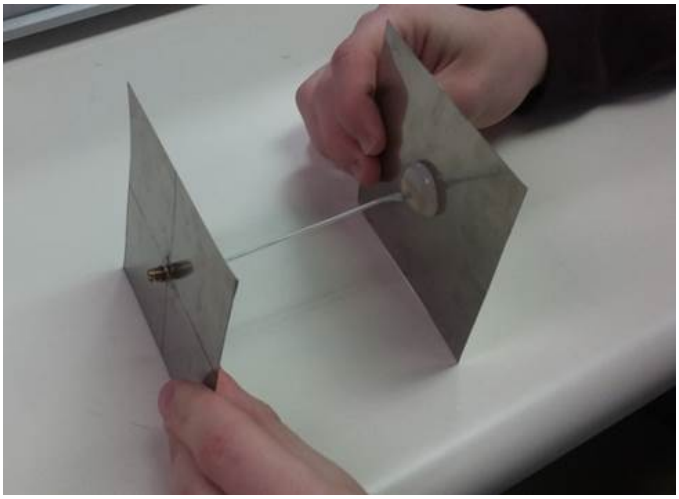

Figure 3.8: Two port scattering parameters measurement setup. The center pin of the lead is connected to the SMA center pins. Both SMAs are placed on a 10 cm by 10 cm aluminum plate that is the ground for the lead. This fixture is placed inside the saline for measurement.

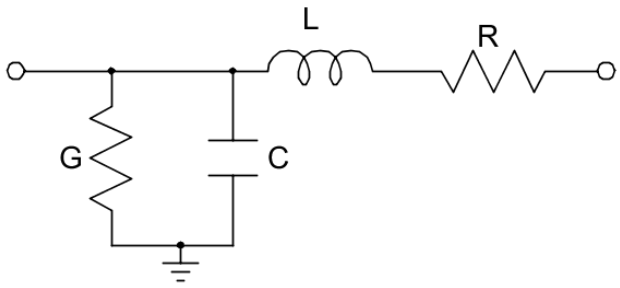

Figure 3.9: Transmission line unit cell that is used to extract the transfer function of the lead.

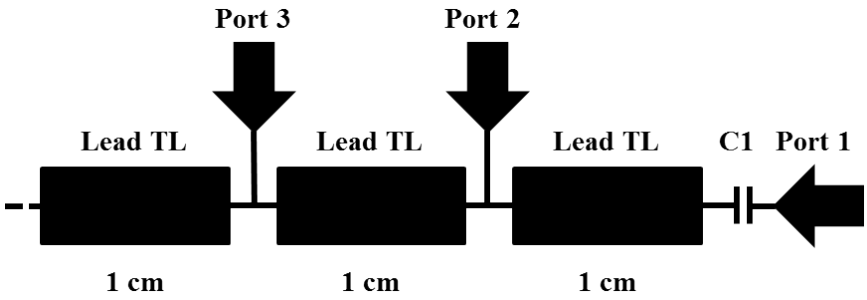

Figure 3.10: Extracting the transfer function of the lead in the circuit simulator. Each unit cell of the lead is equivalent to the measured value of the previous TL models. Capacitor C1 represents the weakly coupling signal to the lead. Port 1 injects the signal to the circuit and other ports measured the receive signal at different positions. By adding different numbers of unit cells, the transfer function of leads for various length can be found.

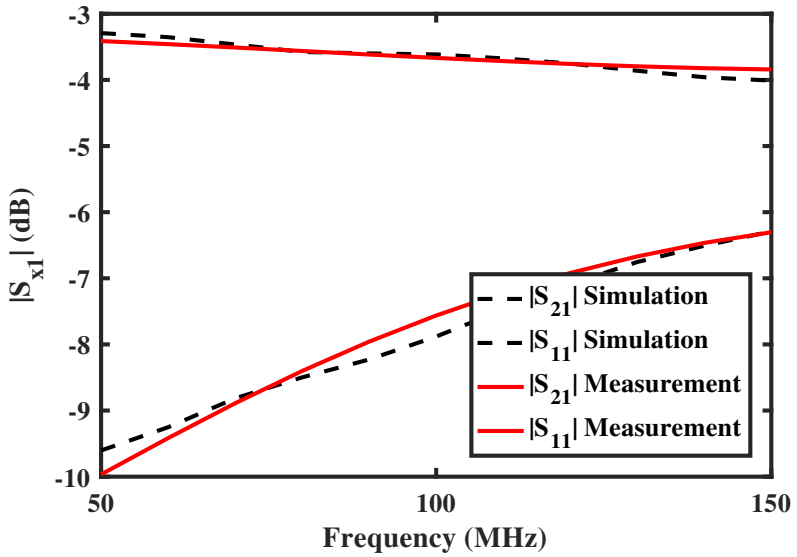

Figure 3.11: Simulation and measurement results of magnitude of scattering parameters that is used to extract the transmission line model of the lead at different frequencies.

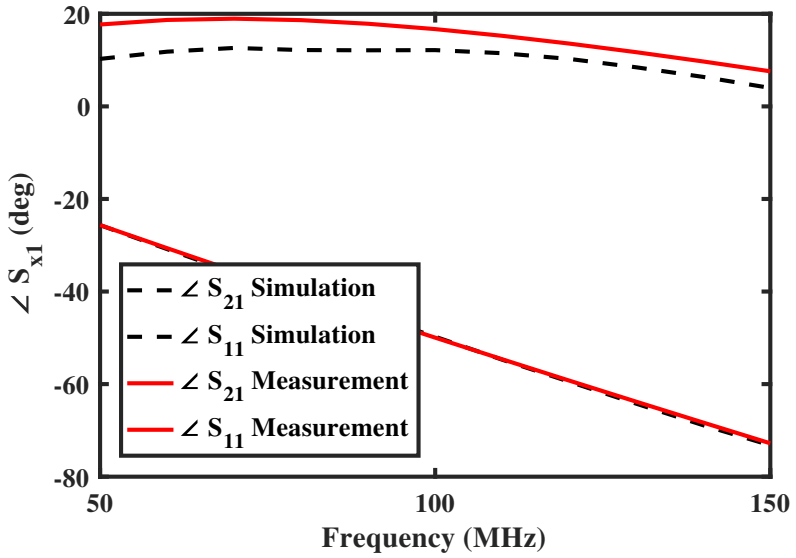

Figure 3.12: Simulation and measurement results of the phase of the scattering parameters that are used to extract the transmission line model of the lead at different frequencies.

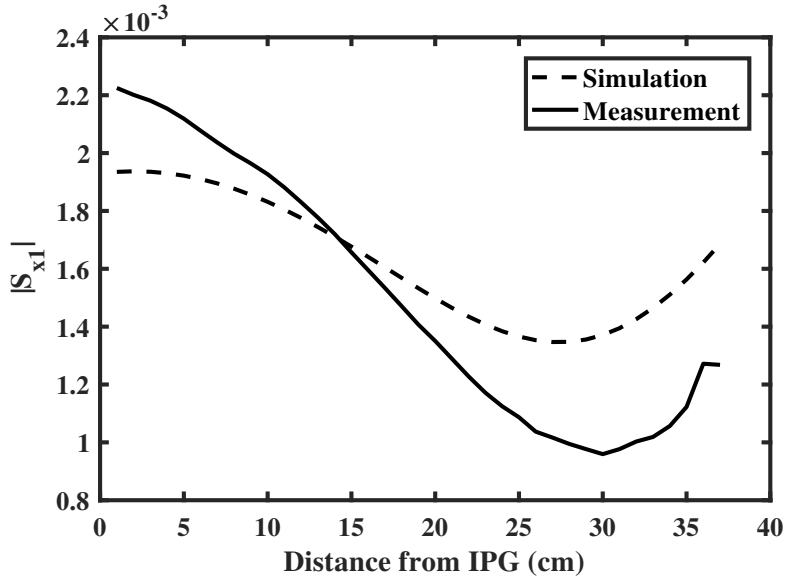

Figure 3.13: Simulated and measured amplitude of the lead transfer function at 64 MHz.

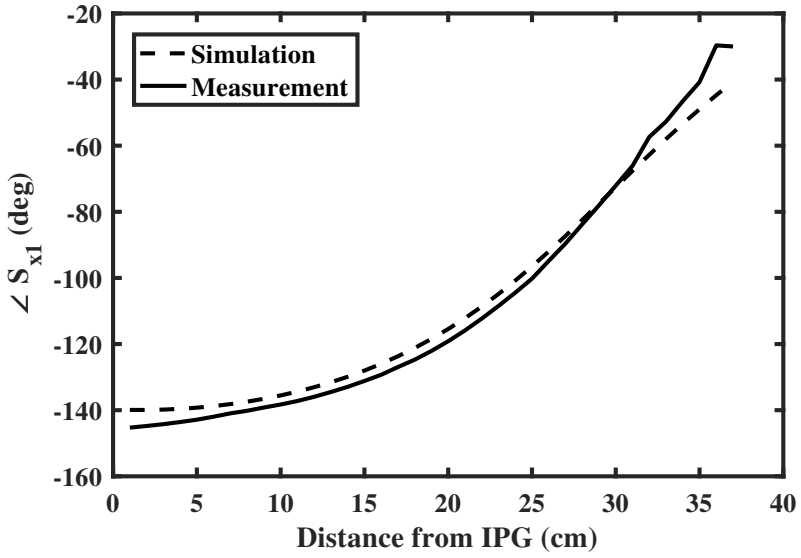

Figure 3.14: Simulated and measured phase of the lead transfer function at 64 MHz.

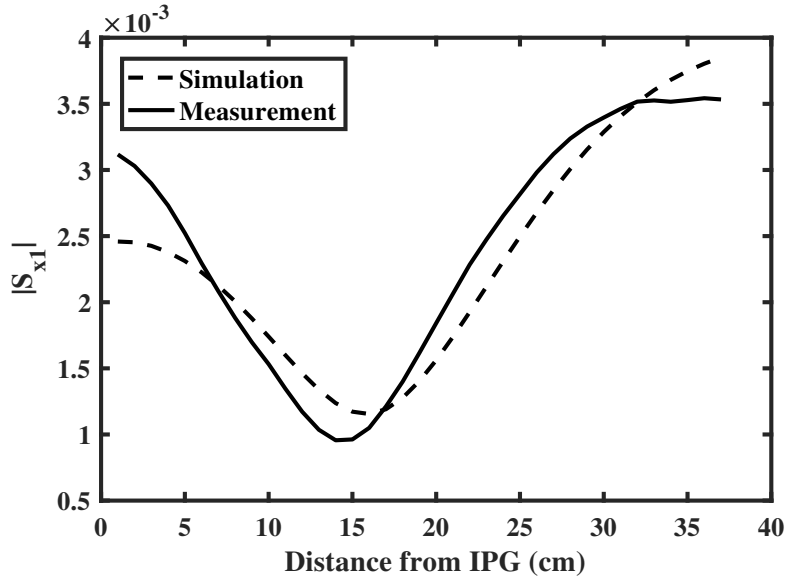

Figure 3.15: Simulated and measured amplitude of the lead transfer function at 128 MHz.

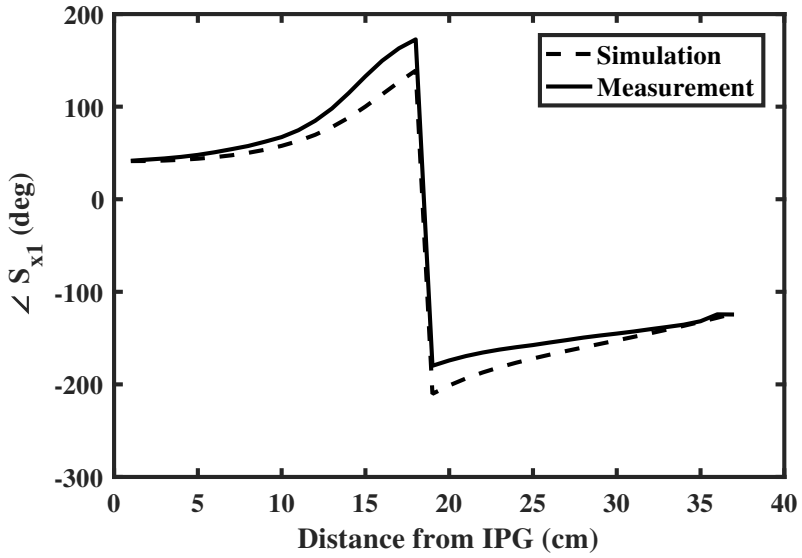

Figure 3.16: Simulated and measured phase of the lead transfer function at 128 MHz.

Chapter 4

Lead characterization

Radiated electromagnetic waves during MRI scanning induce current on the conductive parts of the lead inside human body. The amplitude of the induced currents is a function of the radiated power, the strength of the electrical field at the position of the lead and the electrical properties of the lead. In this chapter a circuit model for implantable devices in the presence of MRI RF waves is proposed. The simulated current distribution on the lead from a 3D EM solver and the proposed circuit model is presented. The unit cell of this circuit model is an expanded model of the lumped element equivalent circuit for an incremental length of transmission line. This model includes the external source that represent the radiated EM wave. Moreover, multiple leads are fabricated and measurement and simulation results are shown.

4.1 Implantable device inside MRI

The RF wave generated during the MRI scan induces current on the conductive parts of the implantable devices. To understand the current on the implantable device, both experiments and advanced EM simulations were performed [4]. It is extremely challenging to solve both the human body and lead models in a 3D EM solver due to the sub-millimeter structure of implantable device

systems.

4.1.1 The lumped element circuit model for a transmission line

Transmission line theory describe the field analysis and circuit theory and therefore is of significant importance in the analysis of RF circuits [40]. Wave propagation on transmission lines can be approached from an extension of circuit theory or from a specialization of Maxwell's equations. Electrical size is the key difference between the circuit theory and transmission line theory [41].

To model the lead inside the human body in the presence of the MRI RF waves, a developed circuit model of the common lumped element TL is presented. As shown in Figure 4.1 (a) the transmission line is schematically represented as the lead and the medium that construct the two conductors of the transmission line. A piece of an infinitesimal length, Δz, of the lead can be modeled as the lumped element circuit shown in Figure 4.1 (b) where the R, L, G and are per unit length quantities defined as follows:

- R = series resistance per unit length, for both conductors, in Ω/m.
- L = series inductance per unit length, for both conductors, in H/m.
- G = shunt conductance per unit length, in S/m.
- C = shunt capacitance per unit length, in F/m.

The series inductance L represents the total self-inductance of the lead's inner conductor and the medium. The shunt capacitance C is due to the close proximity of the two. The series resistance R represents the resistance due to

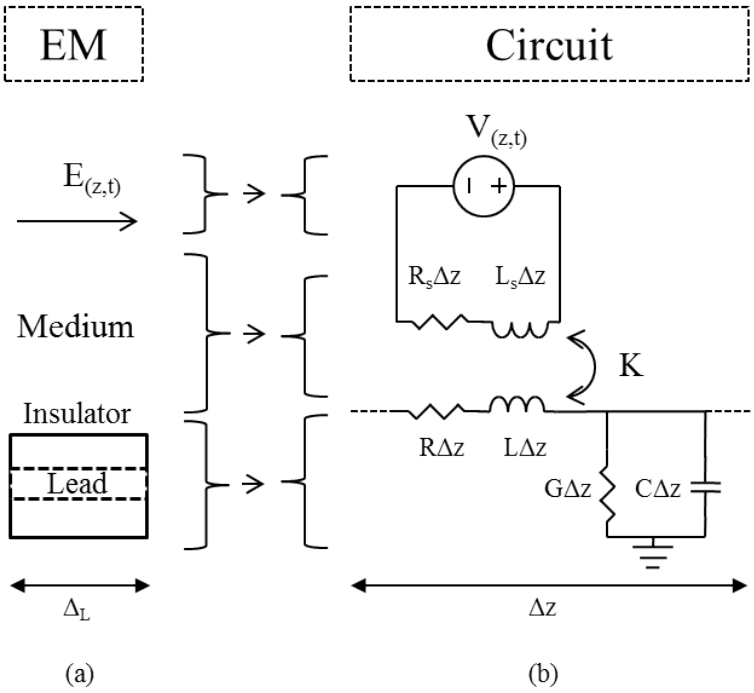

Figure 4.1: Proposed circuit model of the lead. (a) Incremental length of lead inside the human body. (b) Expanded Lumped-element TL model of the lead inside the human body in the presence of the MRI electromagnetic waves. R, L, G and C are the TL parameters. V_s represents the electrical field near the unit cell of the lead and R_s, L_s and K are representing the coupling values of the E-field to the lead.

the finite conductivity of the individual conductors, and the shunt conductance G is due to dielectric loss in the medium or specifically the tissue and insulator between the conductors.

Radiated RF waves that penetrate into the human body during the MRI scan are the source of the current on the lead. As shown in Figure 4.1 (b), another source circuit section is added to the lumped element circuit that represent the coupling mechanism of the RF wave to the lead. This section also provides the flexibility to use the method that is mentioned in chapter 2 to find the TL parameters of the lead.

At any point near the lead, the incident E-field is represented by $E_{z,t}$ in

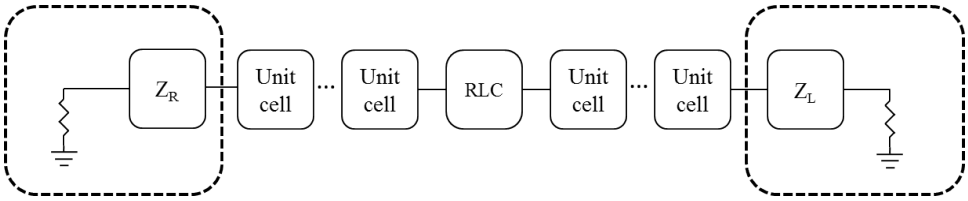

Figure 4.2: General schematic of the lead model and arbitrary position of the RLC network along the lead. Z_R and Z_L are the loads at both end of the lead that represents the electrode, IPG or open circuit.

volts per meter. This field is modeled using a voltage source and represented by $V_{z,t}$. R_s, L_s and K for the resistance, self inductance of the surrounding tissue and the coupling value of the E-field at any point on the lead, respectively.

The TL parameters depend on the lead property which are the insulator and a portion of the surrounding medium, and can be measured, calculated or simulated regardless of the added source section. This is the key point of this model that provides the flexibility to deal with the transmission and the radiation parts of the model independently. Due to the finite conductivity of the medium, the EM wave is attenuated in the direction perpendicular to the lead's surface and the portion that needs to be considered in the TL parameters can be calculated using the skin depth formula as follows [41]

$$\delta = \sqrt{\frac{2\rho}{\omega\mu}} \tag{4.1}$$

where ρ is the resistivity of the medium, ω is the angular frequency of current and $\mu = \mu_r\mu_0$. μ is the degree of magnetization of a material in response to a magnetic field. The μ_r is relative magnetic permeability of the medium and μ_0 is the permeability of free space.

After finding the TL parameters of the lead, the wave propagation parameters can be calculated that will be used to calculate the amount of power that is delivered to the IPG. The characteristic impedance, Z_0, of the lead can be

calculated using

$$Z_0 = \sqrt{\frac{R + j\omega L}{G + j\omega C}}, \tag{4.2}$$

the complex propagation constant from

$$\gamma = \alpha + j\beta = \sqrt{(R + j\omega L)\,(G + j\omega C)}, \tag{4.3}$$

and the wavelength is

$$\lambda = \frac{2\pi}{\beta}. \tag{4.4}$$

4.1.2 Lead in the presence of EM wave

The current distribution on the lead can be predicted using the TL model. A lead that is made using a bare copper wire in air, in the presence of a linear E-field is simulated. The diameter of the wire is 0.5 mm and the length is 40 cm. The EM simulation result and the result of the TL model of the lead are shown in Figure 4.3 at 64 MHz. The equivalent wavelength at this frequency is 4.68 m and the lead length is less than 0.1 λ. Using the same TL parameters of the lead the current distribution is shown in Figure 4.4 at 128 MHz. Decreasing the wavelength of the radiated wave, increases the electrical length of the lead and therefore the amplitude of the maximum induced current. The maximum current is in the middle of the open ended lead, and it is 284 mA and 753 mA at 64 MHz and 128 MHz respectively.

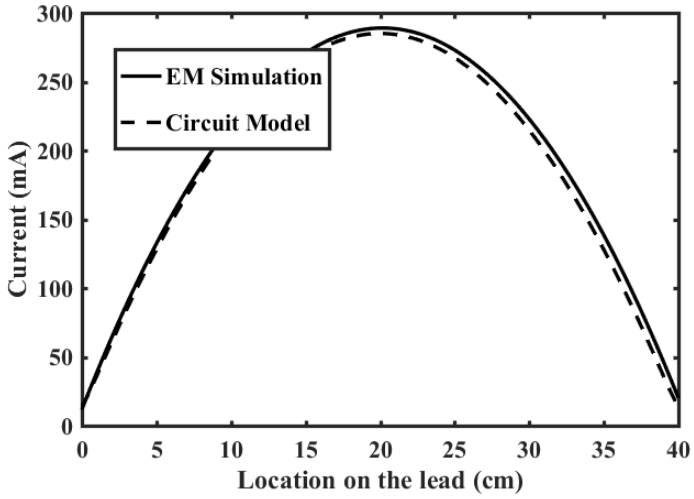

Figure 4.3: Current distribution on the lead in the presence of the MRI EM waves at 64 MHz. The circuit model is shown in Figure 4.2 without the RLC network and open ended lead at both side. The length of the lead is 40 cm and is made of bare copper wire with diameter of 0.5 mm.

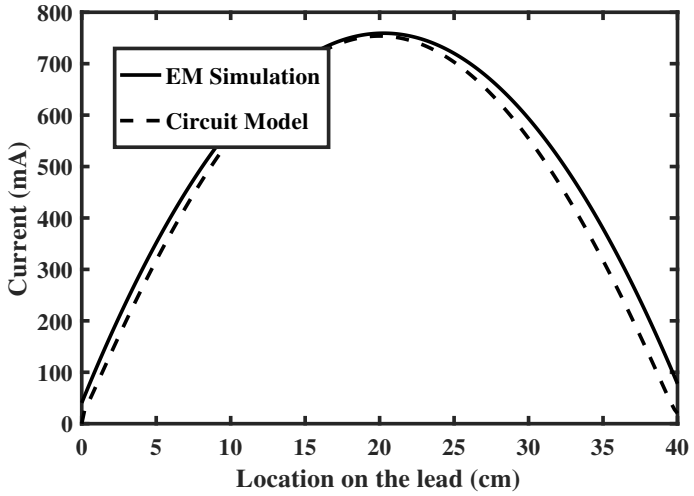

Figure 4.4: Current distribution on the lead in the presence of the MRI EM waves at 128 MHz. The circuit model is shown in Figure 4.2 without the RLC network and open ended lead at both side.The length of the lead is 40 cm and is made of bare copper wire with diameter of 0.5 mm.

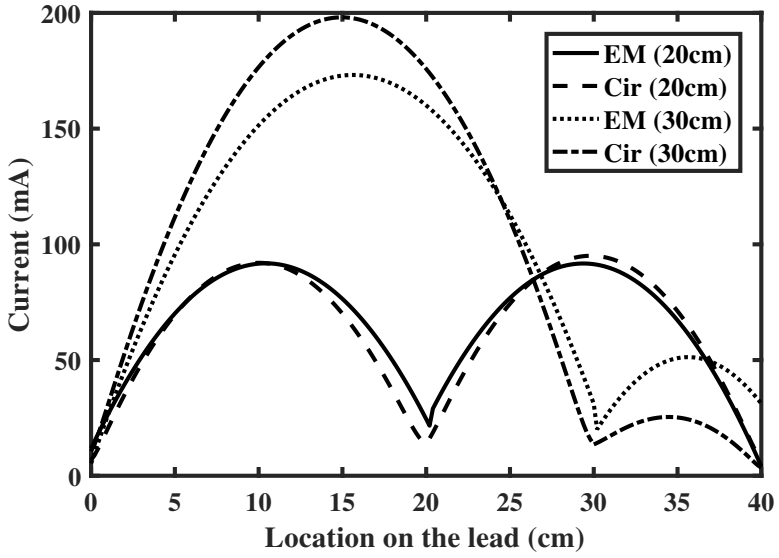

Figure 4.5: Current distribution on the lead in the presence of the MRI EM waves at 64 MHz. Both the EM simulation and the circuit model results are shown. The length of the lead is 40 cm and it is made of a bare copper wire with a diameter of 0.5 mm. A resistor is placed at 20 cm and 30 cm from the left side of the lead.

4.2 Circuit model of the lead with an arbitrary position of the RLC network

A general circuit model of the lead with an arbitrary placement of an RLC network along the lead is shown in Figure 4.2. Total length of the lead sees the same surrounding material therefore the unit cell is similar in all the positions. Each end of the circuit model is terminated by Z_R and Z_L, which represent the loads on the lead.

To validate the circuit model of the lead in the presence of a linear EM field, a 10 kΩ resistor is placed at two positions on the lead. The current distribution along the lead using the EM simulation and circuit model is shown in Figure 4.5 at 64 MHz. One resistor is placed at 20 cm. In the second

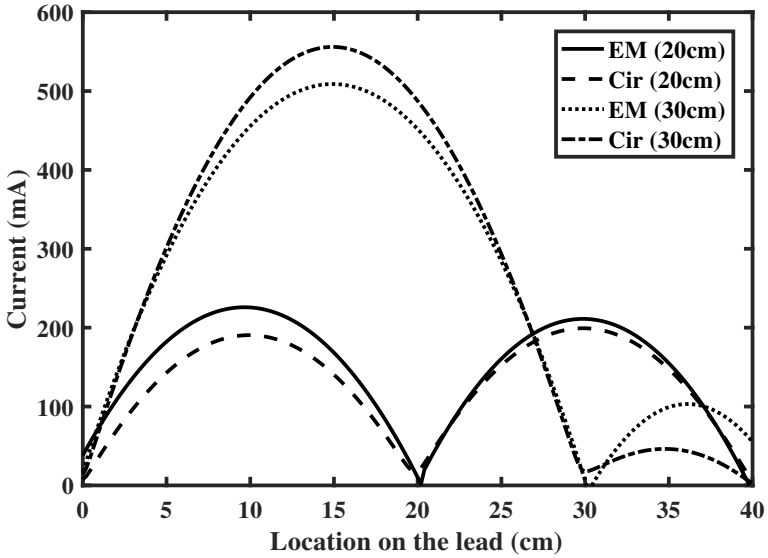

Figure 4.6: Current distribution on the lead in the presence of the MRI EM waves at 128 MHz. Both the EM simulation and the circuit model results are shown. The length of the lead is 40 cm and it is made of a bare copper wire with a diameter of 0.5 mm. A resistor is placed at 20 cm and 30 cm from the left side of the lead.

simulation the resistor is placed at 30 cm. The simulation results at 128 MHz are shown in Figure 4.6. Placing a high impedance resistor at the center of the lead reduces the electrical length around the lead and the maximum current reduces to 92 mA and 225 mA at 64 MHz and 128 MHz respectively.

4.2.1 Circuit model of the lead with IPG

In section 4.2 it was shown that the circuit model predicts the current distribution along the lead. In this section, a 5 cm-diameter IPG is added to the lead. The right side of the lead is an open circuit and therefore the value of Z_R is infinite. On the other side Z_L represent the impedance of the IPG, which is $50 - 80i\ \Omega$. The real part of this impedance is equal to the impedance of the

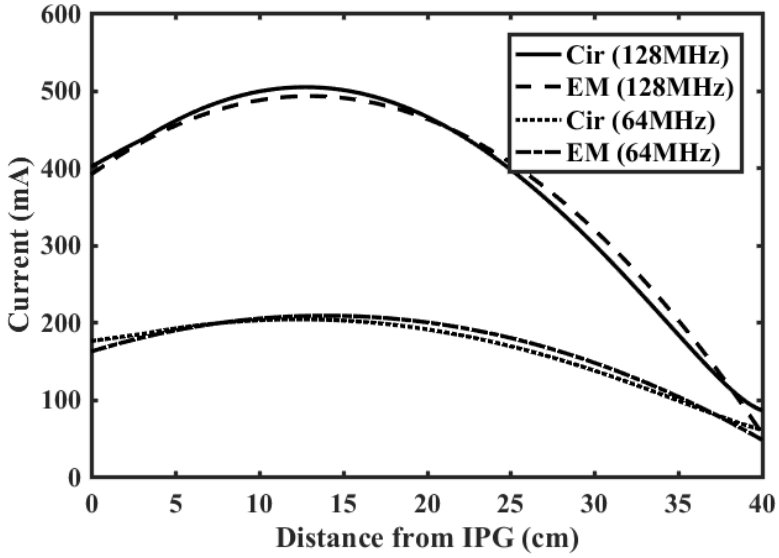

Figure 4.7: Current distribution on the lead that is connected to the IPG in the presence of the MRI EM waves at 64 MHz and 128 MHz. Both the EM simulation and the circuit model results are shown. The length of the lead is 40 cm and it is made of a bare copper wire with a diameter of 0.5 mm.

port that connects the lead to the IPG and the imaginary part is optimized for the current at 64 MHz. The current distribution along the lead, that is connected to the IPG, is shown in Figure 4.7.

The lead is inserted into the IPG and a 50 Ω port is placed between the lead conductor and the IPG case. The current at the input of the IPG is not zero, which is due to the fact that the IPG behaves as the ground plane for the lead.

4.2.2 Implant malfunction

The induced current on the lead during the MRI scan couples to the IPG and can cause malfunction of the implant. The amount of coupling to the IPG depends on the impedance of the lead and the input impedance of the IPG.

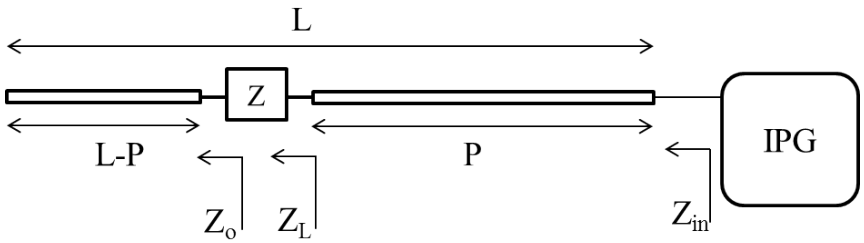

Figure 4.8: Input impedance of the lead with an arbitrary position of the impedance Z. The total length of the lead is L and the distance of the Z from the IPG is P.

To reduce the delivered power to the IPG, the input impedance of the lead can be optimized using a single RLC network. This network can be any configuration of the R, L and C at any position on the lead. The lead can be divided into main four sections as shown in Figure 4.8. The four sections are, open-ended lead, the RLC network represented by Z, another section of the lead, and the IPG. The input impedance of a lossless transmission line with an arbitrary load impedance is

$$Z_{in} = Z_0 \frac{Z_L + jZ_0 \tan(\beta P)}{Z_0 + jZ_L \tan(\beta P)} \tag{4.5}$$

The input impedance of the open-circuited transmission line also can be found using (4.5) where the length of the line is $L - P$:

$$Z_o = -jZ_0 \cot(\beta(L - P)) \tag{4.6}$$

Therefore using (4.6), Z_L is given by

$$Z_L = Z + Z_o = Z - jZ_0 \cot(\beta(L - P)) \tag{4.7}$$

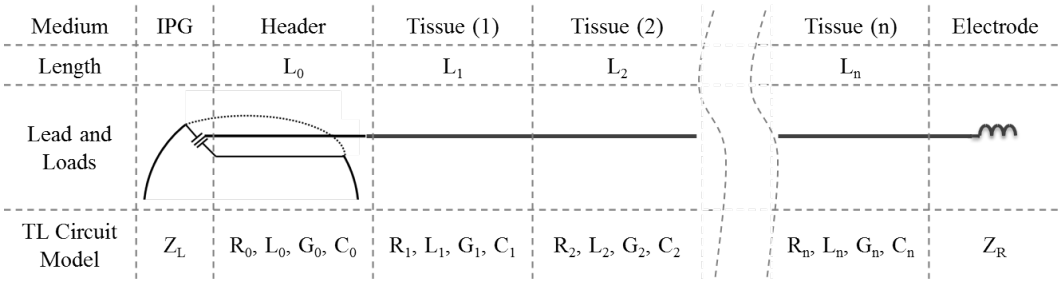

Figure 4.9: Circuit model of an implant inside a human body. The circuit model consists of n+3 sections that include the impedance of IPG, the electrode, and n+1 TL models of the header section and n tissue sections. Each section has a different unit cell and the number of the unit cells depends on the length of the tissue.

using (4.5) with the Z_L from (4.7), the input impedance seen from the IPG is

$$Z_{in} = Z_0 \frac{Z - jZ_0 \cot(\beta(L-P)) + jZ_0 \tan(\beta P)}{Z_0 + Z - jZ_0 \cot(\beta(L-P)) \tan(\beta P)} \tag{4.8}$$

The amplitude of the coupled signal to the IPG is frequency dependent and a patient can have both a 1.5 T and a 3 T MRI, which have the RF frequencies of 64 MHz and 128 MHz, respectively. Using the TL model of the lead, the TL parameters can optimized for all MRI RF frequencies to reduce the possibility of the malfunction.

4.3 General design discussion

The complete circuit model of the entire implantable device inside a human body is shown in Figure 4.9. The lead traverses through multiple tissue layers from the IPG to the Vagus nerve as shown in Figure 1.1. The transmission line parameters of each section of the lead, depends on both the surrounding tissue and the properties of the lead. This model covers all the possible situations

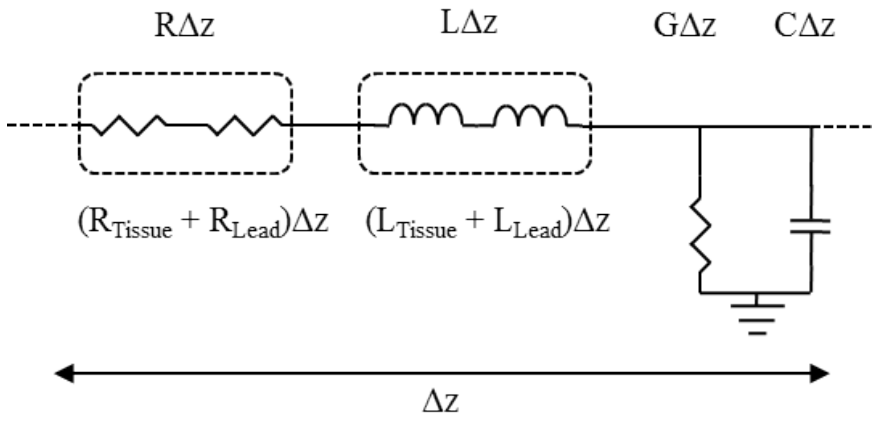

Figure 4.10: Decomposed TL model of the lead inside the human body. This model represents the self resistance and self inductance of the lead as R_{Lead} and L_{Lead}, respectively.

of the lead inside a human body. The TL parameters of the lead is unique for each tissue where they have different length that is represented by L. The first section of the model is based on the header with length L_0. The length and the number of sections depend on the path of the lead inside a human body.

4.3.1 Decomposing the lumped element unit cell of the TL model

The lead of the implantable device is modeled using the proposed transmission line model. This model shows accurate current and voltage distributions along the lead in the presence of an external electromagnetic wave. The most common leads are constructed from one or more internal conductors which are covered with an insulator. Properties of the lead include, but are not limited to, conductivity, length and dimension, all of which vary based on the application. The transmission line parameters depend on both the lead and the surrounding tissue layers that the lead passes through. Figure 4.10 shows

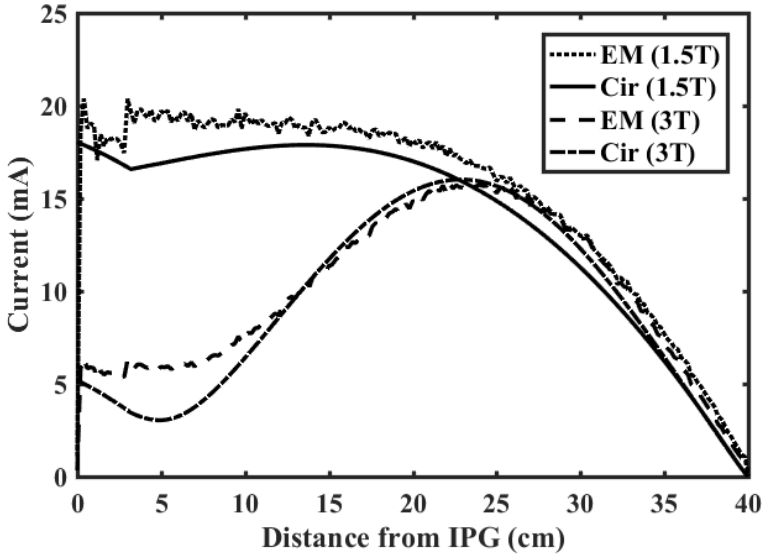

Figure 4.11: Current distribution on the lead with connected IPG inside the saline at 64 MHz and 128 MHz as shown in Figure 4.9. Both EM simulation and circuit model results are shown. The overlap of header and lead are from 0 to 3 cm.

the decomposed lumped element components of the transmission line. Each parameter of the model is divided into two sections, the lead and the tissue. This unit cell shows that, the resistance R, of the TL model is the total resistance per meter of the inner conductor consists of R_{Lead}, and the R_{Tissue} as shown in Equations (4.9) and (4.10). The lead conductor and the surrounding tissue represent the inner and outer conductors of a coaxial transmission line, therefore the resistance per meter of these two are separable. While there is no control of the surrounding tissue, the properties of the TL model that depend only on the lead can be designed to reduce the coupled voltage on the IPG.

$$R(n)\Delta z = \left[R_{Tissue}(n) + R_{Lead}(n)\right]\Delta z \tag{4.9}$$

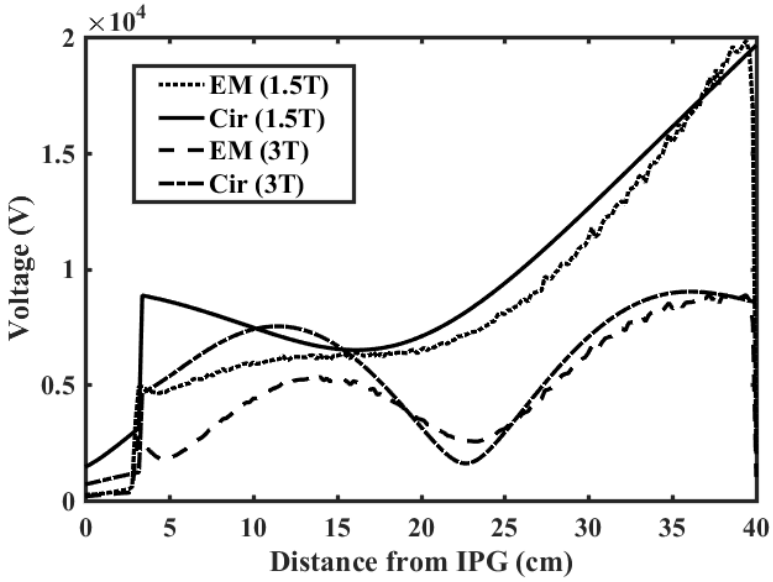

Figure 4.12: Voltage distribution on the lead connected to the IPG inside saline at 64 MHz and 128 MHz. Both EM simulation and circuit model results are shown. The overlap of header and lead are from 0 to 3 cm.

$$L(n)\Delta z = \left[L_{Tissue}(n) + L_{Lead}(n)\right]\Delta z \tag{4.10}$$

The step by step method to model the implant can be explained as follow:

1. Measure the TL parameters of the lead based on the 2 port scattering parameters method introduced in chapter 2. This method is limited to the situation where the total length of the lead is placed in one surrounding material. The TL parameters of the lead can be derived also based on the circuit model introduced in this chapter. This method can be used when the lead passes through multiple tissues. To find the current distribution on the lead, this method requires EM simulation of the lead.

2. Simulate of the IPG and lead, using an EM simulator to find the optimized values of Z_L and Z_R.

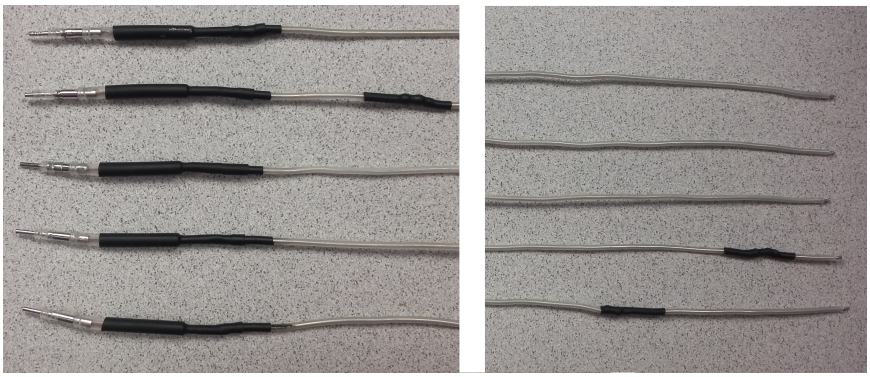

Figure 4.13: Fabricated prototypes of the lead.

3. Simulate the lead, IPG and electrode in the presence of the radiated E-field using an EM simulator to find the $V_{z,t}$, R_s, and L_s in the circuit model.

4. Use equations (4.9) and (4.10) to optimize the position of the resistor on the lead.

4.3.2 Measurement results and discussion

To validate the circuit model of the lead in the presence of the MRI RF waves, multiple prototypes are fabricated, as shown in Figure 4.13, and the measurement results are shown. The inner conductor is a solid tinned copper wire with the diameter of 0.5 mm. The length of the lead is 40 cm. Clear flexible Polyolefin is used as the insulator with a diameter of 1 mm. The electrical length of the unit cells should be less than 0.1 λ. The first 16 unit cells model the lead in the header. The index n in (4.9) is proportional to the distance from IPG.

The coupled voltage on the IPG is measured using a high impedance probe when it is connected to different leads with various positions of a 260 Ω resistor. The voltage is measured using the high impedance coaxial method explained

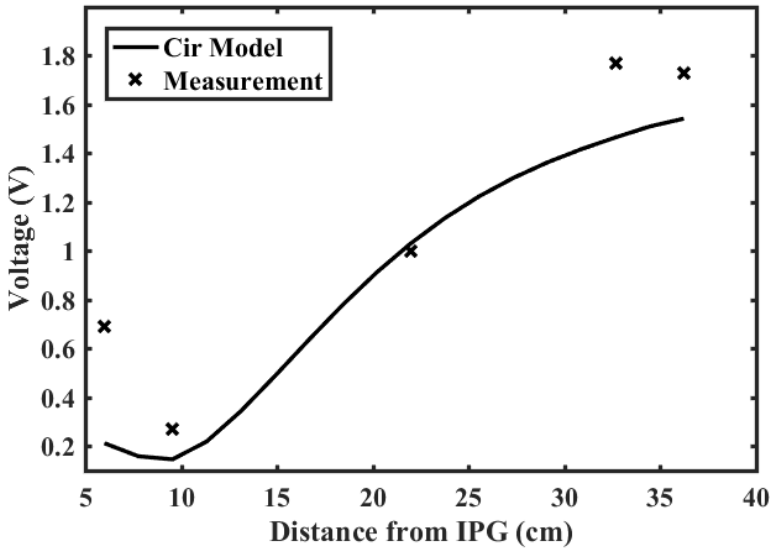

Figure 4.14: Measurement and simulation result of coupled voltage on the IPG versus the position of the resistor in along the lead in the 1.5 T MRI RF birdcage.

in chapter 2. Figure 4.14 shows the measured coupled voltage with 5 different leads to the IPG in 1.5 T MRI and simulated results from the circuit model. The measured and simulated results in 3 T MRI are shown in Figure 4.15.

In this chapter a circuit model of the implant inside a human body in the presence of MRI RF wave is introduced. This model predicts the current and voltage along the lead in different scenarios of implant usage. It is demonstrated that using the decomposed lumped element of the TL model, the placement of a resistor along the lead can be optimized for reducing the implant malfunction. Moreover, this model provides the flexibility of designing the lead independently of the surrounding tissue.

Designing a lead based on the absolute values of the TL parameters, requires a complex mathematical analysis of the lead structure inside the human body. However, the method introduced in this chapter, provides two degrees

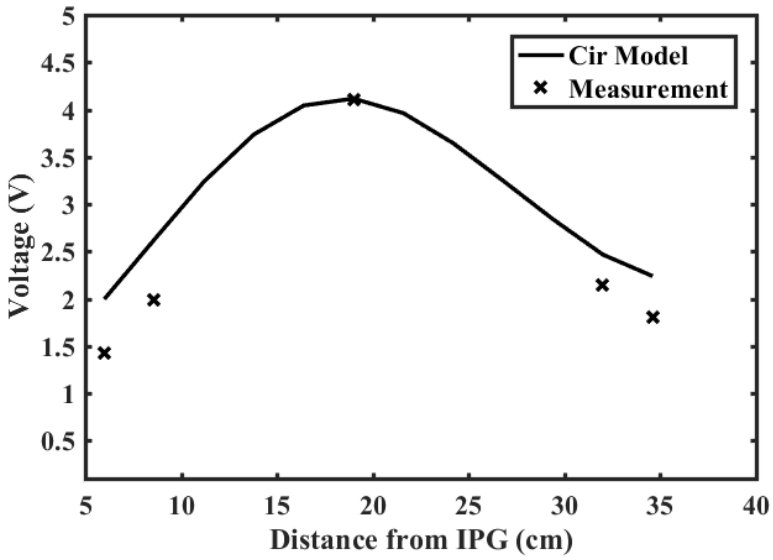

Figure 4.15: Measurement and simulation result of coupled voltage on the IPG versus the position of the resistor along the lead in the 3 T MRI RF birdcage.

of freedom in improving an existing lead using a relative basic design.

Chapter 5

IPG RF front-end in MRI

There are multiple reasons for needing a communication link between implantable devices and an external device and an antenna is the key element of this link. A tablet is used as the external devise for changing settings and transferring data which are two of the most important remote operations. A common method of communication to implantable devices is to use coupled inductors. This method provides a near-field communication link that requires an additional device between the implant and the external device.

In this chapter, two antennas are designed for communication to an implant using Bluetooth technology. This method provides the flexibility of using any phone or tablet without the need of an additional external device. Moreover, this method extends the communication range significantly in comparison with near-field method. Sensitivity analysis based on the position of the implantable device inside a human body is simulated. Comparison results are provided to achieve the best solution regarding antenna parameters, ease of fabrication, cost and sensitivity to the surrounding tissue. The antennas are fabricated and the measured results are shown. Finally, the coupled MRI RF signal to an implantable device is simulated and measured results are shown.

5.1 Bluetooth IPG

One important new feature for the next generation of IPGs is the inclusion of Bluetooth (BT) technology for communicating with external devices. The antenna on the IPG is used for transmitting and receiving IPG therapy information using BT RF signals. The Antenna operation is critical for a robust communication link inside the human body.

Due to the proximity of the antenna to the surrounding tissue, it is necessary that the antenna works properly in different human bodies that have different tissue thicknesses. Usually the IPG is placed in fat and between muscle and skin. Five human body models that cover the minimum to maximum range of the tissue thickness around the IPG are used to investigate the antenna performance.

5.2 Computable human phantoms

Five different human body models from the IT'IS foundation are used to measure the thickness of the human body layers [42]. The models are shown in Figure 5.1. Based on the Virtual Population ViP3.0 models of the IT'IS, the computable phantoms are characterized to predict real-world biological and physiological phenomena for any defined patient population. In this study the human bodies that are studied are as listed below:

- Fat
- Duke
- Ella
- Billie

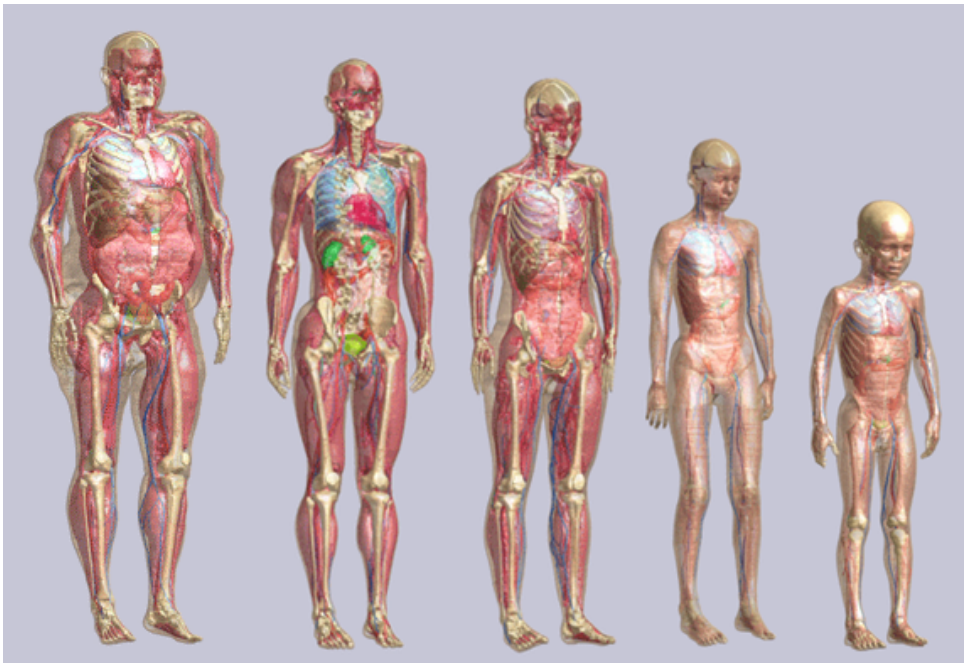

Figure 5.1: Virtual human body models (from [42]). The models from left to right are Fat, Duke, Ella, Billie and Thelonious.

- Thelonious

Names of the virtual human body models and their properties are shown in Table 5.1.

Table 5.1: Demographic of selected virtual human body models (from [42].)

Name	Sex	Age (year)	Height (m)	Weight (kg)	BMI
Fat	male	37	1.82	119.5	36.1
Duke	male	34	1.77	70.2	22.4
Ella	female	26	1.63	57.3	21.6
Billie	female	11	1.49	34.0	15.3
Thelonious	male	6	1.16	18.6	13.8

5.2.1 Sim4Life 3D EM modeler and solver

Sim4Life is a comprehensive set of computable human phantoms empowered by physics solvers and advanced tissue models, providing a realistic biological

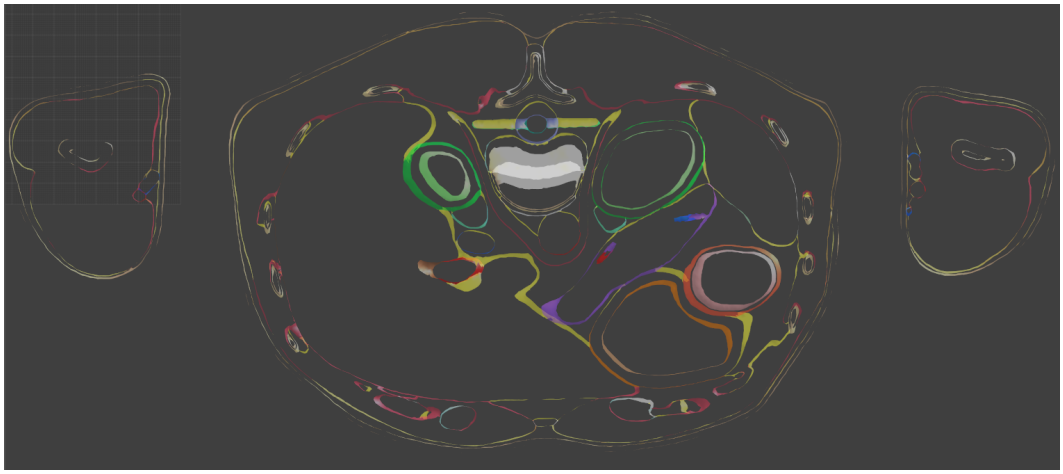

Figure 5.2: A cross section of Duke human body model at position 5 where the IPG is implanted.

and anatomical environment for conducting fundamental mechanistic studies, testing the effectiveness and safety of medical devices and treatments, and supplementing clinical trials [42]. A cross section of human body model that is used for measuring the thickness is shown in Figure 5.2. The image is from the Sim4life software.

5.3 IPG location and thickness measurement

For each human body model, the thickness of the three layers, muscle, fat and skin, are measured at 9 different positions shown in Figure 5.3.

Variation of each layer at different positions in multiple human bodies are provided in Figure 5.4. The total number of measurements is 45, which is equal to the 9 possible positions of IPG in the five human body models. As shown in the statistics summary, the means values of the skin, fat and muscle are 2.24 mm, 11.32 mm and 10.03 mm, respectively.

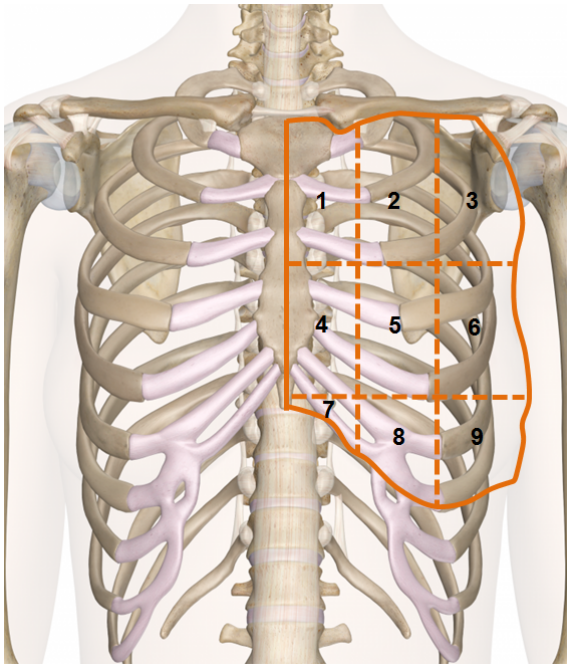

Figure 5.3: Areas/regions of interest for the IPG (from [43])

5.4 Antenna design

To have a robust communication link to implantable devices inside the human body, a link budget calculation, that accounts for all the gains and losses is necessary. This calculation considers all the attenuation due to the antenna feed-line, the matching network inside the IPG, the propagation of the signal through the header, the human body layers (fat, muscle and skin) and air, as well as the antenna gains. The minimum required distance to be able to communicate from an external device to the implant is 2 m. The external device is a tablet and the transmitter and receiver information is extracted from the data sheet. The position and environment of the patient are taken into account in the link budget, which includes both line of sight and non-line

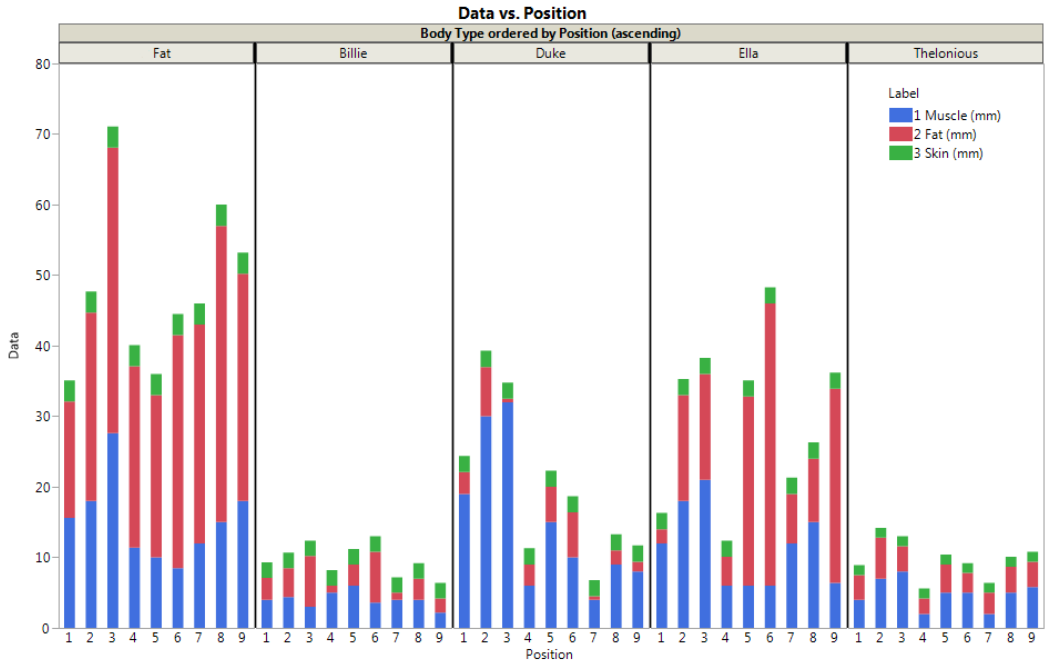

Figure 5.4: Measured thickness layers inside human body model for fat, skin and muscle.

of sight conditions. The link budget equation is:

$$Rx\,(dB) = Tx\,(dB) + Gain\,(dB) - Losses\,(dB) \tag{5.1}$$

The transmitted power from the implant is 5 dBm and the receiver sensitivity of the external device is -80 dBm. The link budget analysis, for all the possible situations, concluded that the antenna peak gain, including human body losses, should be more than -30 dB.

Four antennas are designed and simulated. The first two antennas are straight horizontal as shown in Figure 5.5 (a), and straight vertical as shown in Figure 5.5 (b). The IPG antenna in air behaves like a monopole antenna where the IPG case acts as the ground plane. Figure 5.6 shows the current distribution on the antenna. There are two conductive connectors placed in the

header that are used to connect the internal circuitry of the IPG to the lead. The close proximity of these connectors to the antenna makes the distance between them a potentially sensitive parameter for the antenna performance. The antenna length is quarter wave based on the monopole antenna design. However, in this case due to the lack of the enough ground plane, the length need be optimized. The optimized length of the antenna is 28.1 mm. The permittivity of the header is 3.6 and the IPG is implanted in fat. This is also the maximum possible length of the antenna, due to constraints on the volume of the IPG and the header. To reduce the antenna sensitivity from permittivity changes in the material outside the IPG, a 60 mil clearance to the edge of the header is maintained. The surrounding material depends on the position of the IPG. The thickness of any of the layers varies as shown in Figure 5.4. Having less header material above the antenna and therefore lower overall header volume is the main advantage of the straight horizontal antenna.

To reduce the antenna resonance to the desired frequency, U-shape horizontal antenna is designed as shown in Figure 5.7 (a). However the capacitance between the two section of the U reduces the effective length of the antenna and therefore shifts the resonance to higher frequencies. Another U-shape vertical antenna is designed to reduce overlap between the antenna and the connector block as shown in Figure 5.7 (b). By increasing the space between the components in the header, this design improves the sensitivity in manufacturing. Moreover, in this configuration the distance between the two sections of the antenna is 2.35 mm, which is 4 times larger than the space between the antenna sections in the U-shape horizontal antenna. This spacing reduces the capacitance between the two sections of the U and therefore has less impact

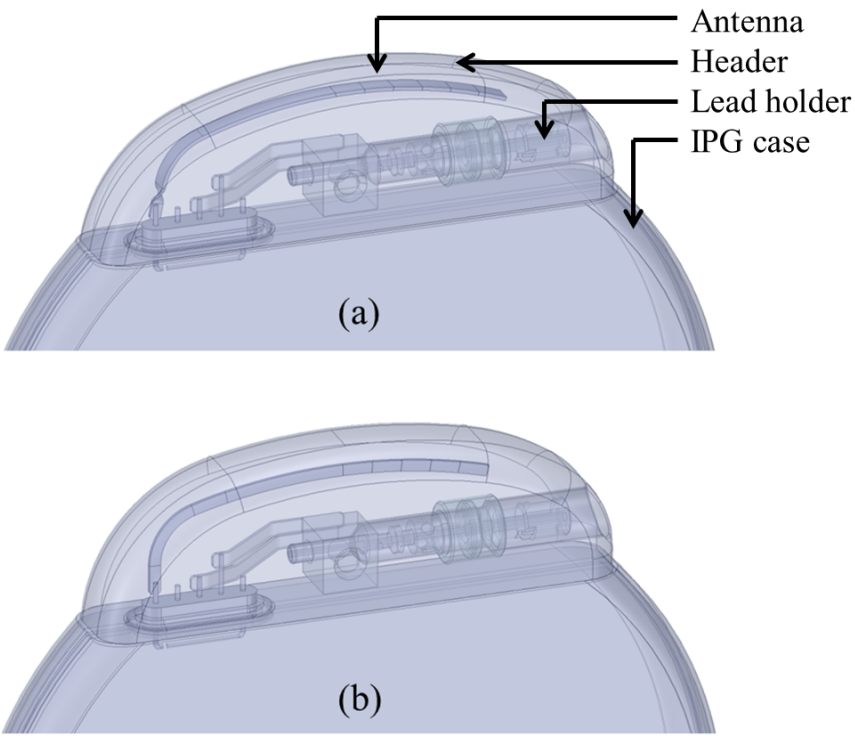

Figure 5.5: Position of the antenna inside the header of the IPG. (a) Straight horizontal antenna in the default header. (b) Straight vertical antenna with tall header.

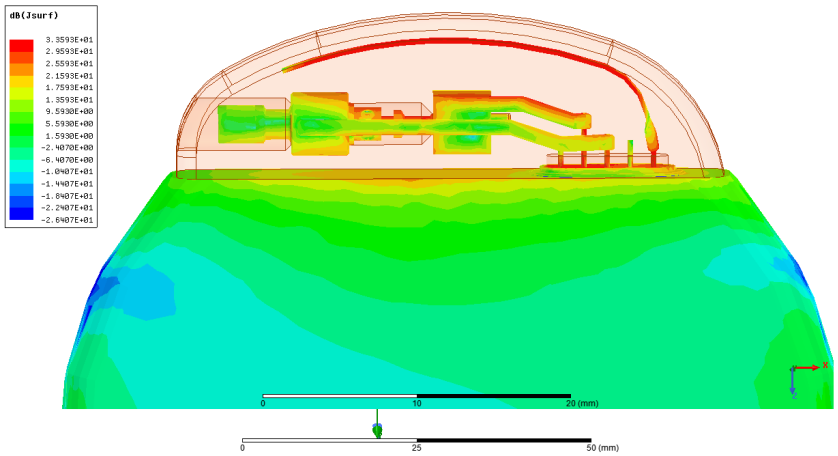

Figure 5.6: Simulated results of the current distribution of the IPG antenna at 2.45 GHz that shows induced current on the components inside the header.

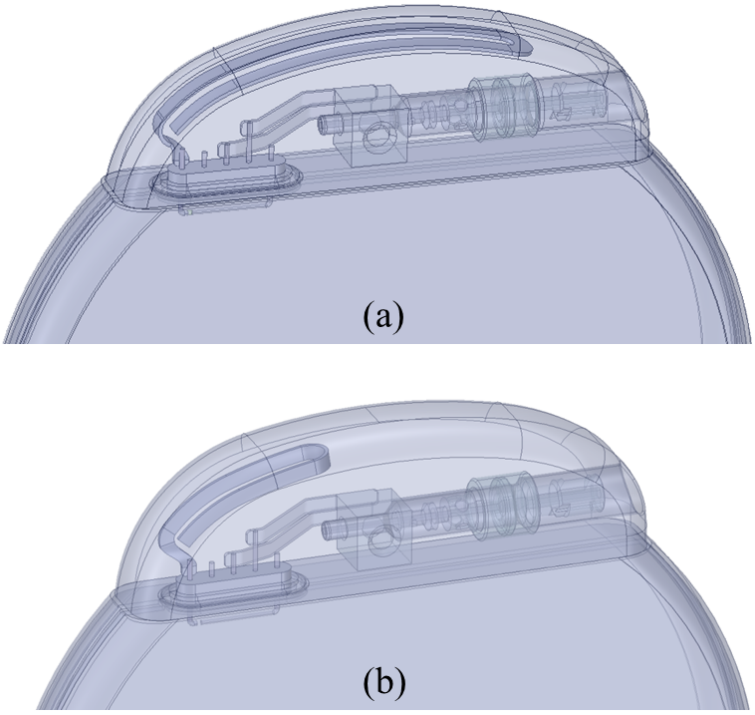

Figure 5.7: Position of the U-shape antennas inside the header. (a) U-shape horizontal and (b) U-shape vertical.

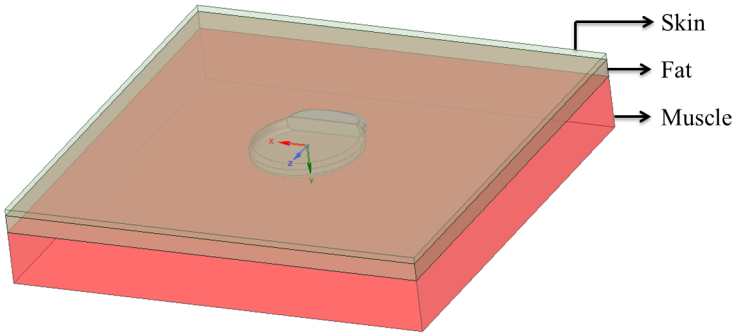

Figure 5.8: 20 cm by 20 cm three layer phantom for antenna simulations that consists of skin, fat and muscle layers from top to bottom. The IPG is placed in the center of the fat layer.

on the effective antenna length. The antenna is simulated with the implant in different configurations. Figure 5.9 shows the 20 cm by 20 cm three layer phantom that is simulated in HFSS. The layers from top to bottom are skin, fat

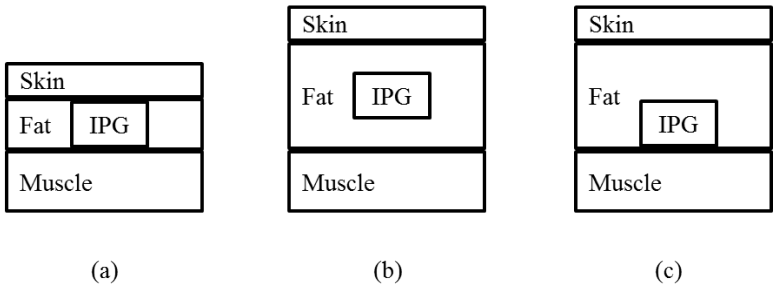

Figure 5.9: Side view of the multilayer phantom with different thickness used for the antenna simulation. a) Thin: skin and muscle thicknesses are 2.5 mm and 25 mm respectively. The minimum thickness of the fat is equal to the thickness of the IPG here which is 8 mm. b) Center: same skin and muscle thickness and the fat thickness is 25 mm. c) Thick: same thickness as (b) where the IPG is placed on the muscle.

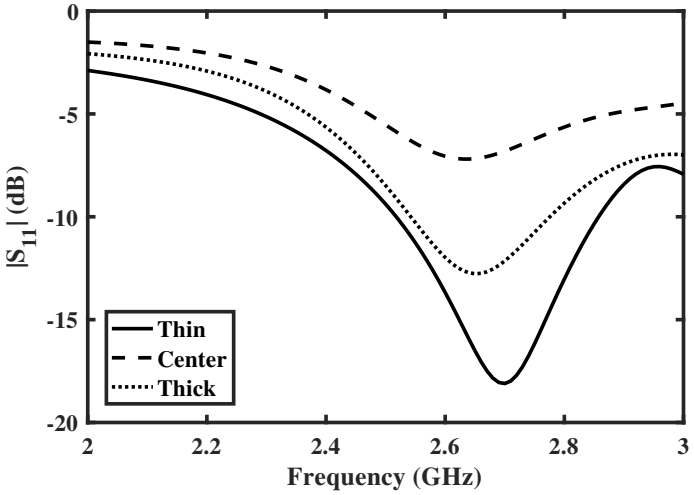

Figure 5.10: Simulated S_{11} results of the sensitivity analysis of the straight vertical antenna in the Thin, Center and Thick configuration.

and muscle. The IPG is placed in the center of the fat layer. Figure 5.9 shows the side view of Figure 5.8 and the thickness variation of the different layers. The three most likely positions of the IPG are represented. Figure 5.9 (a) shows the minimum thickness of the fat layer, which is called the Thin layer. In this configuration the IPG is sandwiched between the skin and muscle layers

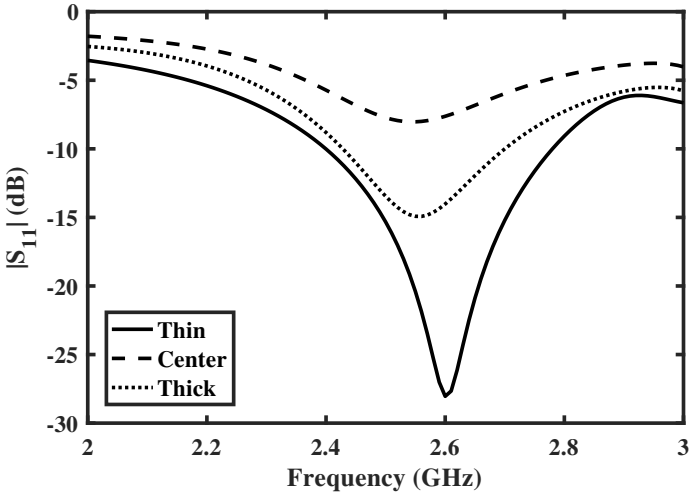

Figure 5.11: Simulated S_{11} results of the sensitivity analysis of the straight horizontal antenna in Thin, Center and Thick configuration.

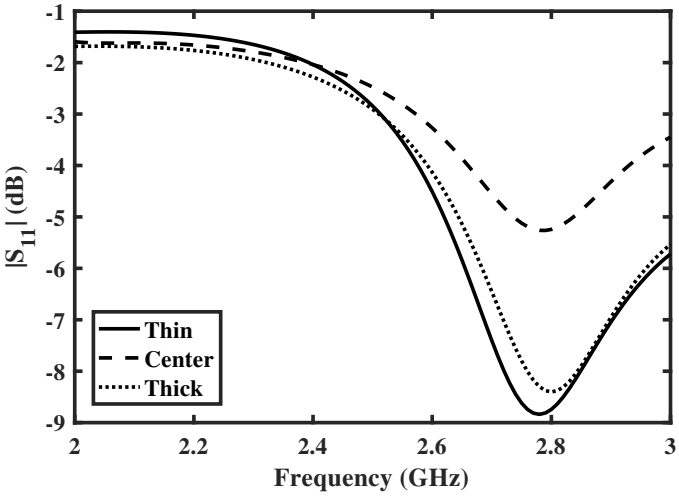

Figure 5.12: Simulated S_{11} results of the sensitivity analysis of the U-shape vertical antenna in the Thin, Center and Thick configuration.

and there is no fat on top and bottom of the IPG. The thickness of the case of the IPG is 8 mm and thickness of the skin and muscle layers are 2.5 mm and 25 mm, respectively. Figure 5.9 (b) shows the configuration with the IPG

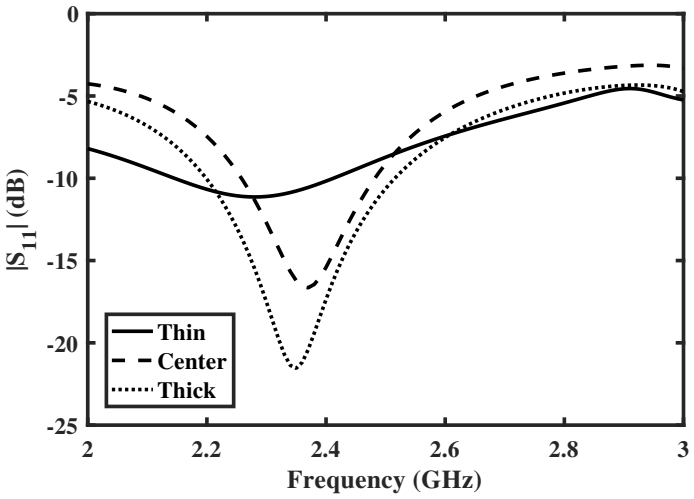

Figure 5.13: Simulated S_{11} results of the sensitivity analysis of the U-shape horizontal antenna in the Thin, Center and Thick configuration.

floating in the fat layer. This position is named Center. The thickness of the skin and muscle layers are the same as for the Thin layer, and the thickness of the fat layer is 25 mm. Figure 5.9 (c) shows the situation when the implant is placed on the muscle layer. The thicknesses of the layers are the same as for the Center configuration. This configuration is called Thick.

5.4.1 Sensitivity analysis

The antenna performance depends on where the IPG is placed inside the human body. This is due to the proximity of the antenna to the adjacent tissue. All the antennas are simulated in different situations to cover a wide range of possible positions. Figure 5.9 shows three different configuration of the IPG. S_{11} of the straight vertical antenna is shown in Figure 5.10 for the three configuration. The permittivity and bulk conductivity of muscle are 52 and 1.73 S/m, respectively, based on [44]. These parameters are 5.2 and 0.1 S/m

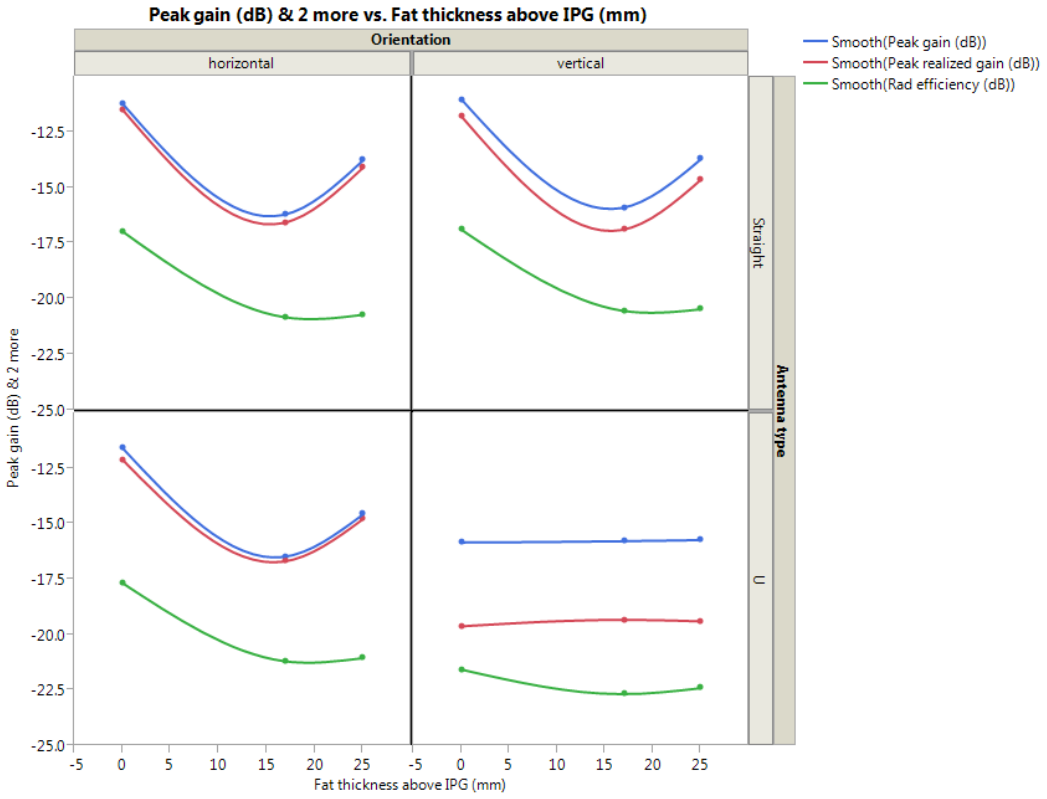

Figure 5.14: Simulated antenna sensitivity results. Simulated results of the straight and U-shape antennas in Thin, Center and Thick phantoms. Horizontal axis shows the thickness of the fat above the IPG that corresponds to the Thin, Center and Thick phantom from left to right respectively.

and 40 and 1.46 S/m for fat and skin, respectively. Due to the significant difference in the permittivity of fat versus muscle the maximum frequency shift occurs when the IPG is in the Center position. The resonant frequency of this structure varies by 2.66 % from 2.63 GHz to 2.7 GHz and the -6 dB bandwidth varies from 230 MHz to 600 MHz. The straight horizontal antenna is also simulated in the same configuration and the results are shown in Figure 5.11. The resonant frequency of this structure varies by 2.36 % from 2.54 GHz to 2.6 GHz and the -6 dB bandwidth varies from 280 MHz to 670 MHz.

The U-shape vertical antenna is shown in Figure 5.7 (b). Figure 5.12 shows the sensitivity simulation results of this antenna. The center frequency of this

Figure 5.15: Fabricated implantable device with the straight vertical antenna. A coaxial cable for the antenna measurement is inserted to the can at the bottom.

antenna changes by 4.4 %. The simulation results of the U-shape horizontal antenna are shown in Figure 5.13. Due to the strong E-field between the two sections of the antenna in this configuration, the S_{11} varies significantly in comparison with the other configurations. Moreover, it is challenging to maintain the distance between two antenna sections constant during manufacturing.

In the link budget analysis, the main antenna parameters of interest are the peak gain, peak realized gain and radiation efficiency. These parameters are shown in Figure 5.14. The maximum peak gain, peak realized gain and efficiency for the straight vertical antenna are -11.04 dB, -11.80 dB and -16.88 dB, respectively, when the antenna is in the Thin layer. For the same configuration, these parameters are -15.83 dB, -19.61 dB and -21.56 dB for the U-shape vertical antenna and -11.59 dB, -12.11 dB and -17.67 dB for the U-shape horizontal antenna.

5.5 Fabrication and measurement

An implantable device with the straight vertical antenna is fabricated and shown in Figure 5.15. The antenna material is stainless steel in a flat ribbon

shape. The length and thickness of the antenna are 2.81 cm and 0.25 mm, respectively. The width of the antenna is 0.76 mm. All the connector blocks are placed in the header and they are shorted to the can after the feed-through insulator. These connectors provides the connections from the internal IPG circuitry to the lead, and they are short circuited at high frequencies with an EMI filter inside the can. Two stainless steel flat ribbons connect these connectors to the feed-through pins. The header material is a medical grade, aromatic, polyether-based, thermoplastic polyurethane (TPU) called Tecothane. This material has a permittivity of 3.8 and a dielectric loss tangent of 0.01. The remaining holes in the header are backfilled during the final manufacturing assembly process. A feed-through insulator is placed between the can and the header, which hermetically seals the titanium case. The feed-through has three pins that connect the internal circuit to the outside of the can. One pin is the ground pin, one is floating and it reserved for future use, and the last pin is connected to antenna. The insulator material is alumina 96pct with a permittivity of 9.4 and a dielectric loss tangent of 0.006. The two titanium halves of the can are connected together using copper adhesive for these prototypes. This will be laser welded in final production. The header is fabricated using injection molding.

The simulated and measured antenna radiation pattern at 2.45 GHz in air are shown in Figure 5.17. The measured antenna peak gain in different scenarios are shown in Table 5.2. The IPG antenna is measured in air, Thin and Thick circular phantom fat. The measurement setup in the antenna chamber is shown in Figure 5.18.

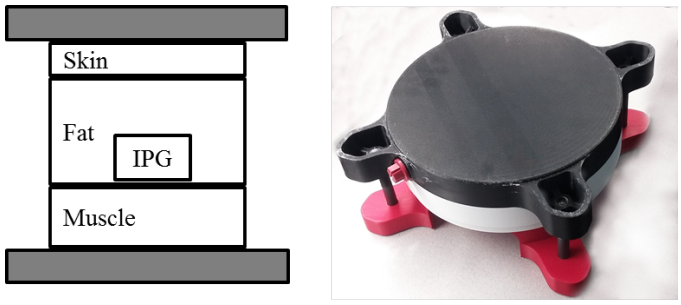

(a) (b)

Figure 5.16: Multilayer circular phantom measurement setup. a) Side view of the internal layers of the phantom. b) Real circular phantom that is fabricated using 3D printing method.

Table 5.2: IPG antenna peak gain measurements summary

IPG Antenna	Scenario	Peak Gain (dBi)
1	air	-0.44
2	Thin fat	-15.99
3	Thick fat	-27.64

5.6 MRI coupled signal to the implant antenna

Implantable devices with antennas are vulnerable to MRI RF. The RF signal couples to the antenna and can cause malfunction of the device. The amplitude of the coupled signal into the antenna depends on multiple factors, such as the antenna radiation pattern, the efficiency, the gain at the MRI frequencies, and the position of the implantable device inside the human body. While the antenna is designed for 2.4 GHz and the gain is greatly reduced in the 20 MHz to 300 MHz frequency range, there is no EMI filter to short circuit the RF signal to the can. High power RF energy is used in MRI to produce images. The radiated power can exceed 46 dBm and 60.2 dBm at 1.5 T and 3 T, respectively. The frequency of the RF signal depends on the strength of the

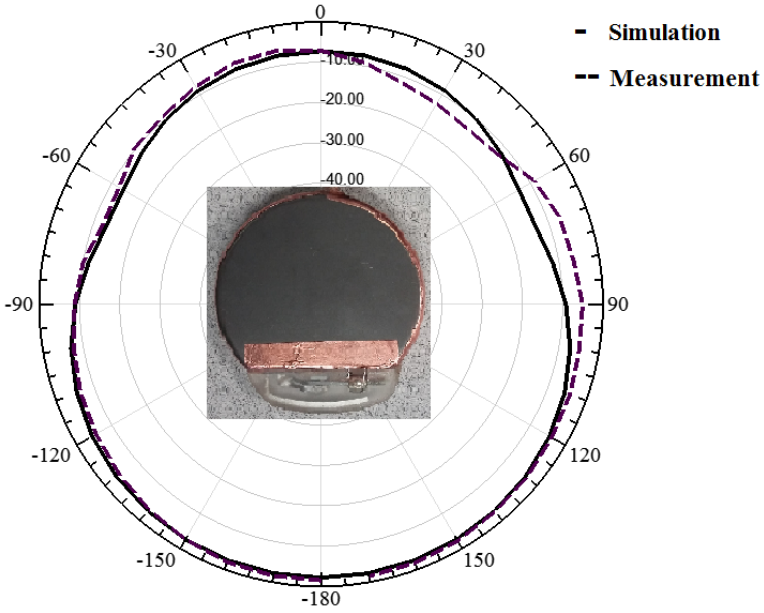

Figure 5.17: Simulated and measured results of the antenna radiation pattern in air at 2.45 GHz.

magnet and it is equal to the Larmor frequency, which is

$$f_0 = \gamma B_0. \tag{5.2}$$

where f_0 is the precession frequency, B_0 is the strength of the externally applied field, and γ is the gyromagnetic ratio, a constant specific to each specific nucleus or particle [45]. The frequencies of the RF signal are 63.87 MHz and 127.74 MHz at 1.5 T and 3 T MRI, respectively. Figure 5.19 shows the summary of the magnitude of the transmission parameters S_{1x} in dB versus the position of the IPG where the x is measurement port number and IPG antenna port is labeled as 1. This MRI RF birdcage has four ports and sixteen radiators.

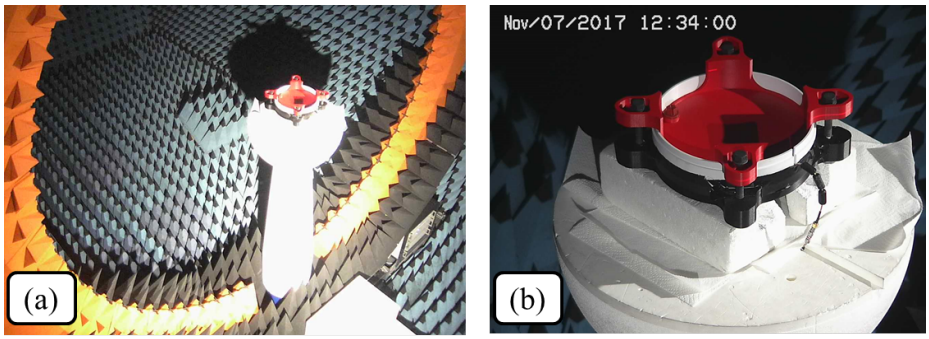

Figure 5.18: Antenna measurement setup in multilayer fat. (a) IPG prototype is SATIMO chamber (b) Multilayer circular fat.

Y \ X	-200	0	200
-150	-66.68	-67.63	-72.37
0	-72.31	-73.92	-75.38
150	-66.16	-67.13	-72.99

Figure 5.19: Simulated results of the coupling to the antenna in the MRI RF birdcage as the function of the position of the IPG. The X and Y quantities are in mm and data are in dB. The color scales show the comparison of the amplitudes.

5.6.1 Coupled MRI RF wave to the antenna

In addition to the coupling to the implant through the leads, the RF signal couples to the implant through the Bluetooth antenna. This port does not have an EMI filter. The prototype antenna, as shown in the Figure 5.15, is designed for the 2.45 GHz ISM band. The IPG is placed inside the birdcage at the position shown in Figure 2.2 (a) and (b). The coupled signal is measured for different RF power levels. Figure 5.20 shows the received power on the antenna port versus the radiated power from the birdcage. The maximum power levels coupled to the antenna port are -21.05 dBm for 64 MHz, where the maximum radiated power is 46 dBm, and -8.38 dBm for 128 MHz, where the radiated power is 60.2 dBm. The power handling of the transceiver module

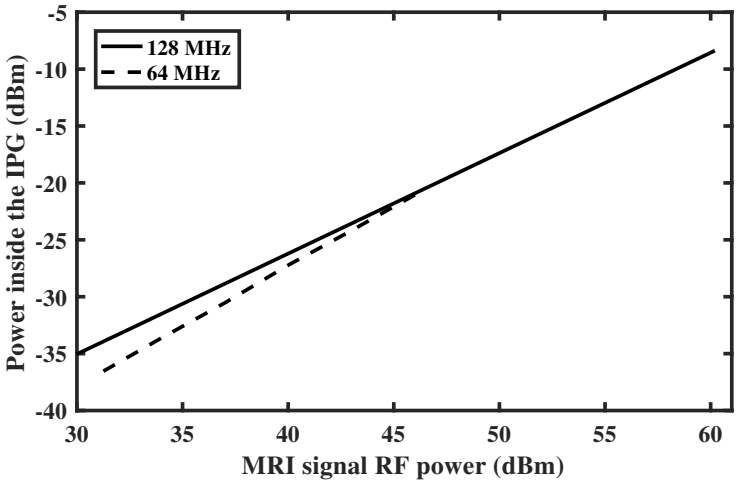

Figure 5.20: Measured RF power inside the IPG versus the radiated RF power from the MRI RF birdcage at the antenna port at 64 MHz and 128 MHz. The IPG placed inside the MRI RF birdcage at $X = 0$ and $Y = 150$ based on the Figure 5.19.

should be greater than the coupled MRI RF power to the antenna port. This measurement provides the limitation for power handling of the transceiver module.

5.7 Conclusion

In this chapter thickness variation of human body models for implantable devices is provided. Four antennas are designed and sensitivity analysis regarding the thickness variation are shown. It is shown that the straight vertical antenna provides a robust solution regarding the human body variation and manufacturability. This antenna is fabricated and simulated and the measured results are provided. Moreover, the antenna is simulated at the MRI frequencies and the coupled power into the antenna during the MRI scanning is measured.

Chapter 6

Conclusion and future work

The goal of this research was to model the implantable device interaction with MRI RF waves during the scanning of patients. First, a circuit model that provides the transfer function of the lead was introduced. This circuit model was based on the transmission line model of the lead. The transmission line parameters of the lead were derived by a new 2 port method in saline. Using this method, the transfer function of the lead was extracted and validated using the measurement. This method significantly simplifies previous methods for measuring the transfer function by removing the need for a complex mechanical setup. Moreover, this method provides the capability to predict the transfer function of the lead for different lengths. This substantially reduces the cost of product development by eliminating the need for new leads. While the measurement results are only shown for 1.5 T and 3 T MRI, having the transmission line parameters can provide the transfer function at any strength of magnetic field.

The second emphasis was on developing a new method for evaluating the possibility of malfunction in the implantable pulse generator during MRI scanning. A small form factor measurement setup, based on an Internal RF Power Detector (IRPD), was designed and implemented. The power detector was

calibrated using the MRI RF signal. A microcontroller was used to convert the voltage from the detector and record the data in an internal memory. The RF field near the implant is not affected by using a completely internal circuit in the implant. This results in an accurate measurement in the MRI, which is the main advantage of this method. Moreover, measuring the coupled power provides an accurate evaluational parameter to estimate the IPG malfunction. The IRPD is shielded from the strong RF fields and can be used in any MRI. The IRPD was designed and implemented on a printed circuit board of the same size as the original IPG board.

The placement of the Vagus Nerve Stimulator (VNS) IPG inside a human body was studied and an antenna for communication to the implant at 2.45 GHz ISM band was designed and implemented. The antenna sensitivity with respect to the human body variation was simulated and a circular phantom that represents the human model was designed and used for the measurements. This design provides a robust, cost effective and a fabrication friendly procedure for IPG. Also, the antenna port vulnerability to the MRI RF signal was investigated since there is no EMI filter on the port. The IRPD was used to measure coupled RF power in different MRIs. This method provides an accurate minimum power level that, transceiver modules, should be able to handle during MRI.

Finally, a circuit model that represents the interaction of the implant with the MRI RF field was introduced. A conventional transmission line model was expanded to model the external radiated E-field. The EM and circuit model simulations in different possible situations of the implant were presented. The model accurately predicts the current and voltage distribution along the lead in on order of thousands of times faster than using EM simulations. This

advantage makes the new lead design significantly cost effective. Moreover, this model was built upon the transmission line model of the lead that eliminates the direct modeling of usually complex structure of it to find the electrical properties. A parsed transmission line unit cell was introduced that distinguish the tissue and lead conductor effects and can be used to design a new lead.

In conclusion, the work presented here introduced new state-of-the-art methods for modeling implantable devices and the expansion of the fundamental concepts of transmission line theory, for addressing challenges associated with current and future MRI technologies.

6.1 Future work

The work presented in this dissertation can be expanded in the following areas.

6.1.1 Simultaneous RF power measurement

It was shown that the IRPD can be used accurately to measure the coupled RF power to the implant on the antenna and lead ports. However, for any measurement to extract the data from the internal memory, the IPG case needs to be opened. Moreover, the RF path from the antenna or the lead to the IRPD needs to be changed for every measurement. Some of the implants can have more than 16 ports and that increases the measurement time extensively. The IRPD can be improved by adding an RF switch on the board. This improvement provides the capability to measure the coupled power to all ports of the implant simultaneously, which will significantly reduce the measurement time. Also, in this case, due to the increasing data, adding an external memory to the microcontroller will be necessary.

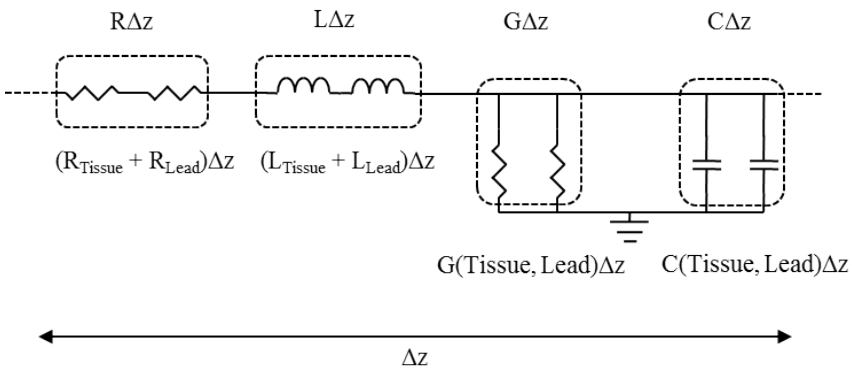

Figure 6.1: Parsed transmission line model of the lead inside a human body. This model represents the self resistance and self inductance of the lead as R_{Lead} and L_{Lead}, receptively, and shows the C and G as a function of lead and tissue.

6.1.2 Expanding the parsed transmission line model

The parsed transmission line model of the lead inside a human body is used to decompose the resistance and self inductance parameters of the lead and provides two degrees of freedom when designing a new lead. The induced current and voltage along the lead can be calculated relatively to the lead, that is being measured, by changing the two aforementioned parameters. However, the model can be improved by the model shown in Figure 6.1. In this model the conductance and capacitance per unit length are a function of both the tissue and the lead as well. This model will provide four degrees of freedoms for designing a new lead.

References

[1] P. Nordbeck, F. Fidler, I. Weiss, M. Warmuth, M. T. Friedrich, P. Ehses, W. Geistert, O. Ritter, P. M. Jakob, M. E. Ladd, *et al.*, "Spatial distribution of rf-induced e-fields and implant heating in mri", *Magnetic resonance in medicine*, vol. 60, no. 2, pp. 312–319, 2008.

[2] S. O. McCabe and J. B. Scott, "Cause and amelioration of MRI-induced heating through medical implant lead wires", in *21st Electronics New Zealand Conference (ENZCon)*, 2014.

[3] X. Mo, C. Jiang, J. Ding, F. Zhang, and L. Li, "Study of deep brain stimulation lead resonant length in 3.0 t mri rf magnetic field", *Electronics Letters*, vol. 52, no. 13, pp. 1098–1100, 2016.

[4] C. Armenean, E. Perrin, M. Armenean, O. Beuf, F. Pilleul, and H. Saint-Jalmes, "Rf-induced temperature elevation along metallic wires in clinical magnetic resonance imaging: Influence of diameter and length", *Magnetic Resonance in Medicine*, vol. 52, no. 5, pp. 1200–1206, 2004.

[5] C. Jiang, X. Mo, J. Ding, Y. Dong, F. Zhang, H. Hao, and L. Li, "Deep brain stimulation lead design to reduce radio-frequency heating in mri", *Electronics Letters*, vol. 50, no. 25, pp. 1898–1900, 2014.

[6] C. J. Yeung, P. Karmarkar, and E. R. McVeigh, "Minimizing rf heating of conducting wires in mri", *Magnetic resonance in medicine*, vol. 58, no. 5, pp. 1028–1034, 2007.

[7] P. Vernickel, V. Schulz, S. Weiss, and B. Gleich, "A safe transmission line for mri", *IEEE transactions on biomedical engineering*, vol. 52, no. 6, pp. 1094–1102, 2005.

[8] *VNS Therapy introducing the aspiresr*, `http://http://www.aspiresr.com/index.html`, Accessed: 2017-06-01.

[9] R. Das and H. Yoo, "Rf heating study of a new medical implant lead for 1.5 t, 3 t, and 7 t mri systems", *IEEE Transactions on Electromagnetic Compatibility*, vol. 59, no. 2, pp. 360–366, 2017.

[10] S. McCabe and J. Scott, "Technique to assess the compatibility of medical implants to the rf field in mri", in *Microwave Conference (APMC), 2015 Asia-Pacific*, IEEE, vol. 2, 2015, pp. 1–3.

[11] M. K. Konings, L. W. Bartels, H. F. Smits, and C. J. Bakker, "Heating around intravascular guidewires by resonating rf waves", *Journal of Magnetic Resonance Imaging*, vol. 12, no. 1, pp. 79–85, 2000.

[12] C. J. Yeung, R. C. Susil, and E. Atalar, "Rf safety of wires in interventional mri: Using a safety index", *Magnetic resonance in medicine*, vol. 47, no. 1, pp. 187–193, 2002.

[13] S. Feng, R. Qiang, W. Kainz, and J. Chen, "A Technique to Evaluate MRI-Induced Electric Fields at the Ends of Practical Implanted Lead", *IEEE Transactions on Microwave Theory and Techniques*, vol. 63, no. 1, pp. 305–313, 2015, ISSN: 0018-9480. DOI: 10.1109/TMTT.2014.2376523.

[14] S.-M. Park, R. Kamondetdacha, and J. A. Nyenhuis, "Calculation of mri-induced heating of an implanted medical lead wire with an electric field transfer function", *Journal of Magnetic Resonance Imaging*, vol. 26, no. 5, pp. 1278–1285, 2007.

[15] J. Hand, "Modelling the interaction of electromagnetic fields (10 mhz–10 ghz) with the human body: Methods and applications", *Physics in medicine and biology*, vol. 53, no. 16, R243, 2008.

[16] V. Acikel and E. Atalar, "Modeling of radio-frequency induced currents on lead wires during mr imaging using a modified transmission line method", *Medical physics*, vol. 38, no. 12, pp. 6623–6632, 2011.

[17] G. Calcagnini, M. Triventi, F. Censi, E. Mattei, P. Bartolini, W. Kainz, and H. I. Bassen, "In vitro investigation of pacemaker lead heating induced by magnetic resonance imaging: Role of implant geometry", *Journal of Magnetic Resonance Imaging*, vol. 28, no. 4, pp. 879–886, 2008.

[18] P. Ehses, F. Fidler, P. Nordbeck, E. D. Pracht, M. Warmuth, P. M. Jakob, and W. R. Bauer, "Mri thermometry: Fast mapping of rf-induced

heating along conductive wires", *Magnetic resonance in medicine*, vol. 60, no. 2, pp. 457–461, 2008.

[19] J. Nyenhuis, J. Jallal, X. Min, S. Sison, and G. Mouchawar, "Comparison of measurement and calculation of the electric field transfer function for an active implant lead in different media", in *2015 Computing in Cardiology Conference (CinC)*, 2015, pp. 765–768. DOI: 10.1109/CIC.2015.7411023.

[20] M. Kozlov and G. Schaefers, "Influence of the second surrounding tissue on radio frequency induced power deposition", in *Antennas and Propagation (APSURSI), 2016 IEEE International Symposium on*, IEEE, 2016, pp. 1635–1636.

[21] P. Soontornpipit, C. M. Furse, and Y. C. Chung, "Design of implantable microstrip antenna for communication with medical implants", *IEEE Transactions on Microwave Theory and Techniques*, vol. 52, no. 8, pp. 1944–1951, 2004, ISSN: 0018-9480. DOI: 10.1109/TMTT.2004.831976.

[22] R. Seman, K. Ghorbani, and Q. Fang, "A new design of circular meander microstrip antenna for on ban system", in *2010 IEEE EMBS Conference on Biomedical Engineering and Sciences (IECBES)*, 2010, pp. 5–8. DOI: 10.1109/IECBES.2010.5742188.

[23] D. Alptekin, N. G. Gençer, and F. Küçükdeveci, "A dual band antenna design for implantable medical devices", in *2014 18th National Biomedical Engineering Meeting*, 2014, pp. 1–3. DOI: 10.1109/BIYOMUT.2014.7026386.

[24] Y. Liu, Y. Chen, and F. H. Juwono, "Differentially fed compact dual-band implantable antenna for biotelemetry", in *2016 IEEE International Symposium on Antennas and Propagation (APSURSI)*, 2016, pp. 1051–1052. DOI: 10.1109/APS.2016.7696233.

[25] C. L. Yang, C. L. Tsai, and S. H. Chen, "Implantable high-gain dental antennas for minimally invasive biomedical devices", *IEEE Transactions on Antennas and Propagation*, vol. 61, no. 5, pp. 2380–2387, 2013, ISSN: 0018-926X. DOI: 10.1109/TAP.2013.2238494.

[26] S. Bakogianni and S. Koulouridis, "Design of a novel miniature implantable rectenna for in-body medical devices power support", in *2016*

10th European Conference on Antennas and Propagation (EuCAP), 2016, pp. 1–5. DOI: 10.1109/EuCAP.2016.7481970.

[27] M. O. Sallam, A. Badawi, and E. A. Soliman, "Design of an implantable miniaturized meander line antenna for biomedical telemetry", in *2016 10th European Conference on Antennas and Propagation (EuCAP)*, 2016, pp. 1–4. DOI: 10.1109/EuCAP.2016.7481309.

[28] K. Y. Yazdandoost, "A 2.4 ghz antenna for medical implanted communications", in *2009 Asia Pacific Microwave Conference*, 2009, pp. 1775–1778. DOI: 10.1109/APMC.2009.5384240.

[29] Z. J. Yang, S. Q. Xiao, L. Zhu, B. Z. Wang, and H. L. Tu, "A circularly polarized implantable antenna for 2.4-ghz ism band biomedical applications", *IEEE Antennas and Wireless Propagation Letters*, vol. 16, pp. 2554–2557, 2017, ISSN: 1536-1225. DOI: 10.1109/LAWP.2017.2732460.

[30] M. E. Ladd and H. H. Quick, "Reduction of resonant RF heating in intravascular catheters using coaxial chokes", *Magnetic Resonance in Medicine*, vol. 43, no. 4, pp. 615–619, 2000.

[31] P. Serano, L. M. Angelone, H. Katnani, E. Eskandar, and G. Bonmassar, "A novel brain stimulation technology provides compatibility with mri", *Scientific reports*, vol. 5, p. 9805, 2015.

[32] R Das and H Yoo, "Innovative design of implanted medical lead to reduce mri-induced scattered electric fields", *Electronics Letters*, vol. 49, no. 5, pp. 323–324, 2013.

[33] V. Acikel, A. Uslubas, and E. Atalar, "Modeling of electrodes and implantable pulse generator cases for the analysis of implant tip heating under mr imaging", *Medical physics*, vol. 42, no. 7, pp. 3922–3931, 2015.

[34] T. Barbier, R. Piumatti, B. Hecker, F. Odille, J. Felblinger, and C. Pasquier, "An rf-induced voltage sensor for investigating pacemaker safety in mri", *Magnetic Resonance Materials in Physics, Biology and Medicine*, vol. 27, no. 6, pp. 539–549, 2014.

[35] *Analog devices*. [Online]. Available: http://www.analog.com/en/products/rf-microwave/rf-power-detectors/rms-responding-detector/adl5906.html.

[36] S. Atash-bahar, H. H. Sigmarsson, and D. Thompson, "Implantable neurostimulator lead transfer function based on the transmission line model", in *Antennas and Propagation & USNC/URSI National Radio Science Meeting, 2017 IEEE International Symposium on*, IEEE, 2017, pp. 401–402.

[37] S. Pisa, G. Calcagnini, M. Cavagnaro, E. Piuzzi, E. Mattei, and P. Bernardi, "A Study of the Interaction Between Implanted Pacemakers and the Radio-Frequency Field Produced by Magnetic Resonance Imaging Apparatus", *IEEE Transactions on Electromagnetic Compatibility*, vol. 50, no. 1, pp. 35–42, 2008, ISSN: 0018-9375. DOI: 10.1109/TEMC.2007.915282.

[38] A. Missoffe and S. Aissani, "Experimental setup for transfer function measurement to assess rf heating of medical leads in mri: Validation in the case of a single wire", *Magnetic Resonance in Medicine*, 2017.

[39] Q. Wang, Q. Zeng, and J. Chen, *Cyberonics RF induced heating report*.

[40] R. E. Collin, *Foundations for microwave engineering*. John Wiley & Sons, 2007.

[41] D. M. Pozar, *Microwave engineering*. John Wiley & Sons, 2009.

[42] *Human models*. [Online]. Available: https://www.itis.ethz.ch/virtual-population/virtual-population/overview/.

[43] *Regions of interest for implantable pulse generator*. DOI: CYB02775.

[44] S Gabriel, R. Lau, and C. Gabriel, "The dielectric properties of biological tissues: Ii. measurements in the frequency range 10 hz to 20 ghz", *Physics in medicine and biology*, vol. 41, no. 11, p. 2251, 1996.

[45] R. H. Hashemi, W. G. Bradley, and C. J. Lisanti, *Mri: The basics*. Lippincott Williams & Wilkins, 2012.